DeHNSSo

The Delft Harmonic Navier-Stokes Solver for Nonlinear Stability Problems with Complex Geometric Features

Westerbeek, S.; Hulshoff, S.; Schuttelaars, H.; Kotsonis, M.

DOI
10.1016/j.cpc.2024.109250

Publication date
2024

Document Version
Final published version

Published in
Computer Physics Communications

Citation (APA)
Westerbeek, S., Hulshoff, S., Schuttelaars, H., & Kotsonis, M. (2024). DeHNSSo: The Delft Harmonic Navier-Stokes Solver for Nonlinear Stability Problems with Complex Geometric Features. *Computer Physics Communications*, *302*, Article 109250. https://doi.org/10.1016/j.cpc.2024.109250

Computer Physics Communications 302 (2024) 109250

Contents lists available at ScienceDirect

Computer Physics Communications

journal homepage: www.elsevier.com/locate/cpc

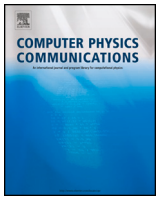

Computer Programs in Physics

DeHNSSo: The delft harmonic Navier-Stokes solver for nonlinear stability problems with complex geometric features ☆,☆☆

S. Westerbeek [a,*], S. Hulshoff [a], H. Schuttelaars [b], M. Kotsonis [a]

[a] Delft University of Technology, Faculty of Aerospace Engineering, Department of Flow Physics and Technology, TU Delft, Kluyverweg 1, 2629 HS, Delft, the Netherlands
[b] Delft University of Technology, Faculty of Mathematics, Department of Applied Mathematics, Mekelweg 4, 2628 CD, Delft, the Netherlands

ARTICLE INFO

Keywords:
Surface imperfections
Boundary layer transition
Nonlinear stability analysis
Harmonic Navier-Stokes
Parabolized stability equations

ABSTRACT

A nonlinear Harmonic Navier-Stokes (HNS) framework is introduced for simulating instabilities in laminar spanwise-invariant shear layers, featuring sharp and smooth wall surface protuberances. While such cases play a critical role in the process of laminar-to-turbulent transition, classical stability theory analyses such as parabolized or local stability methods fail to provide (accurate) results, due to their underlying assumptions. The generalized incompressible Navier-Stokes (NS) equations are expanded in perturbed form, using a spanwise and temporal Fourier ansatz for flow perturbations. The resulting equations are discretized using spectral collocation in the wall-normal direction and finite-difference methods in the streamwise direction. The equations are then solved using a direct sparse-matrix solver. The nonlinear mode interaction terms are converged iteratively. The solution implementation makes use of a generalized domain transformation to account for geometrical smooth surface features, such as humps. No-slip conditions can be embedded in the interior domain to account for the presence of sharp surface features such as forward- or backward-facing steps. Common difficulties with Navier-Stokes solvers, such as the treatment of the outflow boundary and convergence of nonlinear terms, are considered in detail. The performance of the developed solver is evaluated against several cases of representative boundary layer instability growth, including linear and nonlinear growth of Tollmien-Schlichting waves in a Blasius boundary layer and stationary crossflow instabilities in a swept flat-plate boundary layer. The latter problem is also treated in the presence of a geometrical smooth hump and a sharp forward-facing step at the wall. HNS simulation results, such as perturbation amplitudes, growth rates, and shape functions, are compared to benchmark flow stability analysis methods such as Parabolized Stability Equations (PSE), Adaptive Harmonic Linearized Navier-Stokes (AHLNS), or Direct Numerical Simulations (DNS). Good agreement is observed in all cases. The HNS solver is subjected to a grid convergence study and a simple performance benchmark, namely memory usage and computational cost. The computational cost is found to be considerably lower than high-fidelity DNS at comparable grid resolutions.

Program summary
Program Title: DeHNSSo
CPC Library link to program files: https://doi.org/10.17632/9bnms99kk2.1
Developer's repository link: https://github.com/SvenWesterbeek/DeHNSSo
Licensing provisions: GPLv3
Programming language: Matlab
Supplementary material: The supplementary material contains the code as well as a user manual.
Nature of problem: Fluid flows are subject to laminar-to-turbulent transition following the growth of instabilities. To avoid computationally demanding Direct Numerical Simulations (DNS), perturbation theory is often applied to their analysis. However, classical stability methods based on the Orr-Sommerfeld equation or the Parabolized Stability Equations neglect the influence of streamwise gradients in varying degrees. The validity of these assumptions is difficult to estimate a priori.

☆ The review of this paper was arranged by Prof. Peter Vincent.
☆☆ This paper and its associated computer program are available via the Computer Physics Communications homepage on ScienceDirect (http://www.sciencedirect.com/science/journal/00104655).

* Corresponding author.
E-mail address: S.H.J.Westerbeek@tudelft.nl (S. Westerbeek).

https://doi.org/10.1016/j.cpc.2024.109250
Received 7 July 2023; Received in revised form 7 May 2024; Accepted 14 May 2024
Available online 20 May 2024

Solution method: The Delft Harmonic Navier-Stokes Solver (DeHNSSo) solves the harmonic Navier-Stokes equations nonlinearly on domains featuring sharp and smooth spanwise invariant surface features using a generalized grid approach in combination with an embedded boundary method. This allows the user to include the effects of streamwise gradients on flow at a fraction of the cost of DNS.

Additional comments including restrictions and unusual features: In DeHNSSo, the equations are solved using direct matrix solvers. As such, memory is treated as a scarce resource. The problem is formulated in a mode-independent manner such that left-hand side matrices need only be computed and stored once despite incorporating nonlinear terms. Additionally, DeHNSSo offers the user the possibility to prescribe inhomogeneous boundary conditions to introduce and solve the receptivity problem or manipulate instabilities. Due to the double Fourier expansion, the solver is restricted to spanwise and temporally periodic problems.

Nomenclature

x, ξ	Streamwise coordinate (global and computational)
y, η	Wall-normal coordinate (global and computational)
z	Spanwise coordinate (global and computational)
U, u'	Streamwise velocity (base and perturbation)
V, v'	Wall-normal velocity (base and perturbation)
W, w'	Spanwise velocity (base and perturbation)
P, p'	Static pressure (base and perturbation)
$\mathbf{Q}, \mathbf{q}'$	Velocity vectors $[U, V, W]^T$ and $[u', v', w']^T$
$\boldsymbol{\phi}'$	State vector of velocities and pressure $[u', v', w', p']^T$
i	Imaginary unit
α	Streamwise wavenumber
β	Spanwise wavenumber
ω	Angular frequency
A	Maximum streamwise perturbation velocity
h	Protuberance height
H	Domain height
L	Domain length
$\Gamma_{x/y/\eta/\xi}$	Discretization parameter, subscript defines the discretization axis
x_c	Protuberance location
b	Hump width
^{0}	Inflow value
$'$	Perturbation value
$\hat{}$	Shape function
$\bar{}$	Dimensional quantity
*	Integration quantity
$\bar{\delta}_0$	δ_{99} at the inflow
δ_{99}	Boundary layer height based on U
ν	Kinematic viscosity
Re	$\frac{\bar{U}_0 \bar{\delta}_0}{\bar{\nu}}$ Reynolds number

1. Introduction

In a wide range of physical and engineering flows, the laminar-to-turbulent transition is governed by the inception, growth, and breakdown of flow instabilities. For example, flows over aircraft wings normally experience transition due to the growth of instabilities such as viscous Tollmien-Schlichting (TS) waves and inviscid stationary Cross-flow Instabilities (CFI) [1–3]. The location and conditions under which transition occurs are significant as they strongly influence skin friction drag. The field of flow stability analysis is concerned with predicting the onset of transition to turbulence, resulting from the exponential growth of instabilities. These are typically considered as perturbations to a time-invariant base flow solution, which facilitates varying simplifications of the analysis, most notably linearization [4–6]. Although such simplifications can lead to considerable reductions in computational time, they must be balanced by the need to represent the essential underlying physics with sufficient fidelity.

The classical and most widely used approach to stability analysis is the linear quasi-empirical approach. This is based on the Orr-Sommerfeld (OS) equations (e.g. [5,7]), which are derived from the Navier-Stokes equations after introducing a wave-like perturbation solution. A fully local solution is then obtained by assuming that the laminar base flow is parallel, and ignoring the streamwise development (i.e., the history) of the perturbations. Lastly, the amplitudes of perturbations are assumed to be infinitesimal, thus allowing nonlinear interactions to be neglected. The final set of equations can be cast into a homogeneous eigenvalue problem, which can be efficiently solved using either a spatial or temporal formulation [8]. The accumulated linear growth of instabilities can then be correlated with empirical transition location measurements (typically requiring experimental calibration) to find the so-called critical N-factor [9]. The N-factor was initially introduced in a simpler form ($N \approx 9$) by Van Ingen [10] and later by Smith and Gamberoni [11].

While the widespread and continuous use of OS-based LST and e^N methods is a testament to their success, their inherent assumptions limit their applicability to more complex transitional flows. Recognizing this, Bertolotti et al. [12] and Herbert [13] introduced the Parabolized Stability Equations (PSE). In contrast to the derivation of the OS equations, the PSE employ a non-local analysis of the flow, where the shear layer is assumed to be varying, albeit slowly, in the streamwise direction. The slowly-varying flow assumption allows the second-order streamwise derivatives to be neglected, effectively parabolizing the NS equations, and reducing the computational cost of their solution. Furthermore, the nonlinear terms can be maintained as the PSE framework fully accounts for the streamwise development of the perturbation amplitudes necessary for predicting nonlinear interactions.

However, owing to their formulation and set of assumptions, the accuracy and validity of OS and PSE approximations, which neglect higher-order streamwise derivatives, are questioned for a wide range of critically important flows. This is particularly true for the analysis of transitional boundary layers developing over complex surface features such as steps, gaps, humps, and waviness which arise during the fabrication of wings and other geometries. Extensive experimental and numerical studies, such as by Holmes et al. [14], Wang and Gaster [15] and Tufts et al. [16] among others, have attempted to define universal roughness-based Reynolds number thresholds, above which these features become critical, i.e. promote transition. For example, Crouch et al. [17] attempted to find the effect of backward and forward-facing steps on the critical N-factor experimentally. Edelmann and Rist [18] performed a similar study numerically and found that the N-factor reduction is a function of streamwise position, step location, step height, and Mach number. As linear methods were used in the aforementioned studies, perturbation amplitude effects were not considered. For steps in swept-wing boundary layers, Tufts et al. [16] proposed to use the instability's vortex core height and the step height to find the effect on incoming disturbances. However, Eppink [19] and Rius-Vidales and Kotsonis [20] noted that this single-parameter model neglects key aspects of the underlying physics such as the incoming perturbation amplitude. Predicting the effects of geometrical surface features on boundary layer stability requires a deeper understanding and modeling of the underlying flow mechanics. However, the parameter space to be considered is extensive (e.g., Reynolds number, surface geometry, and wave specifications) and demands an efficient modeling approach.

In cases with moderate macro-scale curvature, PSE stability results were found to match experimental results [21]. In other studies, more rapid changes such as localized humps [22–24] and waviness [25–27] were found to significantly affect the stability of the flow so that PSE solutions were not always accurate. Similarly, sharp protuberances such as steps and gaps were shown to strongly affect the dynamics and onset of transition [28–32]. The PSE framework was unable to capture the perturbation behavior in these cases [31]. Moreover, recent experimental and DNS work revealed the possible existence of spatially non-modal effects in the vicinity of such abrupt streamwise changes [19,33,34], which further highlights the limits of the classical modal PSE framework when analyzing these flows. Lastly, Dobrinsky [35] showed that PSE could not provide accurate solutions close to disturbance sources commonly used to introduce or manipulate instabilities. In such cases, a linearized Navier-Stokes approach proved much more effective. It is evident from the aforementioned studies that accurate and efficient modeling of flow stability in complex geometrical domains cannot be reliably performed using a parabolized or local stability framework. In this context, a framework based on the Harmonic Navier-Stokes (HNS) equations is more appropriate when the effects of sharp geometrical features, strong gradients, strong reversed-flow regions, and disturbance sources must be considered [35]. The first implementation of weakly nonlinear (or bilinear) HNS can be found in [36] where the framework was successfully used to predict receptivity of both streamwise and crossflow instabilities in boundary layers over nonuniform surfaces. Another early implementation of *linear* HNS can be found in Streett [37], who aimed at using fast direct linear solvers while maintaining the algorithmic elements of DNS by describing the disturbance field as a set of selected frequencies. The PSE and OS methodologies were shown to underestimate the stabilizing effect of curvature compared to HNS. The HNS methodology was able to capture the effects of curvature and predict the receptivity of crossflow disturbances resulting from wall suction and two-dimensional TS waves resulting from a roughness strip respectively. Guo et al. [38] arrived at a similar conclusion when comparing results for various flows (Blasius boundary layer, swept wing, and swept Hiemenz flow) with PSE solutions. They introduced a streamwise wavenumber in the HNS ansatz, leading to the so-called adaptive approach. A complex streamwise wavenumber was calculated to capture growth and streamwise oscillations in the wave function using an iterative procedure borrowed from the PSE methodology. This reduced the grid requirement significantly at the cost of an additional convergence loop.

In recent years, several studies have demonstrated the capabilities of the HNS framework in various stability problems where classical stability methods fail to provide accurate results. Carpenter et al. [39] formulated and developed a discrete adjoint linear HNS solver to tackle the problem of distributed receptivity on wavy walls in a swept Hiemenz flow. Additionally, the adjoint formulation was used to confirm that the placement of discrete roughness elements is the most sensitive near the neutral point as found in the SWIFT experiments of [40]). Moreover, the importance of surface quality was found through an exhaustive parametric study using the same framework.. Later, Franco et al. [23,29] demonstrated the first compressible adaptive implementation of the Harmonic Linearized Navier-Stokes (HLNS) able to incorporate smooth wall humps. Additionally, sharp geometries were considered using a multi-block approach. As in Guo et al. [38], a streamwise wavenumber was introduced to reduce the grid requirements at the cost of an additional convergence loop. However, the benefit of this approach is likely to be negligible for wall features where the HNS framework is potentially most useful, due to the appearance of non-modal effects not accurately described by a single streamwise wavenumber in the vicinity of the step, as seen in Casacuberta et al. [33]. Zhao et al. [41] used an HLNS approach to study the effect of smooth roughness in the form of humps and dimples on hypersonic boundary layers. The effect of backward-facing steps (corresponding to the experiments of Wang and Gaster [15]) was analyzed with an HLNS approach by Hildebrand et al. [42] where the sharp step geometry was approximated with a cosine function to facilitate the use of a curvilinear grid transformation. The HNS methodology was thus proven capable of incorporating both smooth and sharp surface features.

A further challenge in the HNS approach is to account for nonlinear effects. Although the HNS equations are theoretically capable of accounting for the nonlinear interaction between instability modes, most existing approaches consider the linearized equations. A key issue associated with maintaining the nonlinear terms stems from their iterative convergence, which is typically initiated using a linear solution. In particular, in cases such as simulating CFI, the absence of nonlinear forcing in the first few iterations means that disturbances can grow indefinitely within the considered domain. The subsequent nonlinear forcing from this linear initial estimate can lead to an introduction of higher harmonics that far exceed any physically possible disturbance amplitude, which can lead eventually to solution divergence. Often, damping must be introduced to converge to a nonlinear solution.

To the authors' knowledge, few recent works have been successful in accounting for nonlinear effects within the HNS framework. The doctoral thesis of Appel [43] tackles the fully nonlinear HNS equations in depth using the Harmonic Balance Method (HBM). The interaction of TS waves with a single circular cylinder protruding from the surface was considered nonlinearly, similar to the experiments of de Paula et al. [44]. The development of stationary CFI in a swept-wing boundary layer was also assessed. The nonlinear problem was iteratively solved akin to a nonlinear PSE approach by introducing a source term that contains the nonlinear terms on the right-hand side of the system of equations. The perturbation amplitude was slowly increased in combination with an under-relaxation of the nonlinear terms. A further challenge in the work of Appel [43] was the extensive use of Random-Access Memory (RAM). To reduce memory usage, the sparsity pattern of the left-hand side matrix was used to perform a symbolic LU factorization. This method reduced the RAM requirements, albeit at the cost of computational efficiency.

The work of Rigas et al. [45] used an HNS framework to perform a nonlinear input/output analysis of flat plate boundary layer transition via both K-type and H-type transition. Nonlinear interactions were treated using an implicit formulation akin to the harmonic balance procedures found in Hall et al. [46] and Fabre et al. [47]. A Newton iteration was used to converge the method from a linear initial guess to a nonlinear solution, truncated at four modes in the temporal and spanwise dimensions. The problem was solved using a pre-conditioned Generalized Minimal RESidual (GMRES) method algorithm. Although effective, the method was found to be computationally expensive due to the required calculation of the Jacobian, i.e. finite-dimensional block Hill matrix [48].

Most recently, Scholten et al. [49] employed the fully nonlinear HNS equations to predict the amplification of nonmodal disturbances in a hypersonic boundary layer over a blunt cone. An approach similar to Rigas et al. [45] is employed where the equations are solved with a fully implicit formulation and the Newton-Raphson method requiring the calculation of the Jacobian. The authors also noted the computational constraints and used a GMRES scheme to solve the problem. Excellent agreement with NPSE solutions is found for the planar Tollmien-Schlichting wave in the Blasius flow as well as the development of a planar second Mack mode in hypersonic flow over a cone. The scheme proved robust for high inflow amplitude simulations where convergence issues occurred with the NPSE framework in contrast to findings by Appel [43]. However, the tested cases are not comparable between these two works which could affect the convergence characteristic of the specific method implementations.

Another challenge in the implementation of (harmonic) Navier-Stokes solvers is the handling of the outflow boundary. Unsteady flow disturbances that reach and interact with the outflow boundary can lead to spurious reflections that travel upstream at infinite speeds in incompressible formulations. This has a detrimental effect on the solution

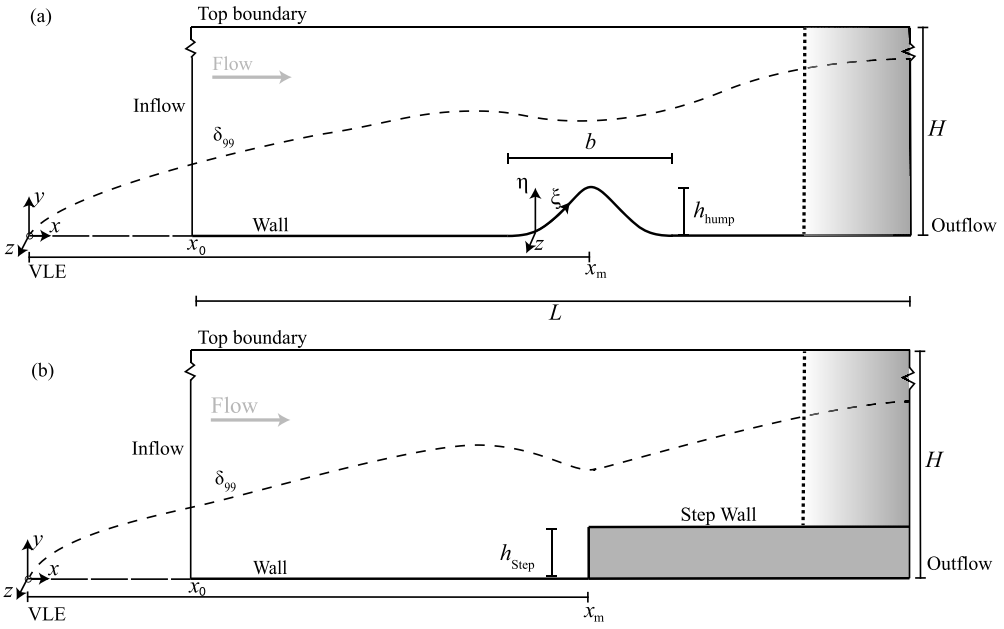

Fig. 1. Example problems showing the Cartesian (x, y, z) and generalized coordinate (ξ, η, z) systems for a smooth hump (a) and step (b) as well as flow direction, feature dimensions, and the virtual leading edge. The outflow buffer is indicated by the shaded region where the attenuation function goes from 1 (white) at the dotted vertical line to 0 (dark grey) at the outflow. For an explanation of the other symbols, see the text.

within the interior domain. This problem has led some researchers to introduce a streamwise wavenumber in the solution ansatz [29,38,50]. By absorbing the wave-like character of disturbances in the wave function, reflections from the interaction at the outflow boundary can be mitigated. Although effective, this method introduces an additional equation to find the wavenumber as done in PSE, e.g. by Bertolotti et al. [12]. Kloker et al. [51] compared various techniques to treat the outflow boundary, ranging from no particular treatment to altering the domain length and flow control options to attenuate disturbances near the outflow, adjusting the Reynolds number, or suppressing disturbance vorticity directly. They concluded that the suppression of disturbance vorticity was most effective. It must be noted that the problem formulation made use of vorticity transport equations, allowing for convenient access to this perturbation property. Appel [43] introduced a sponge layer based on a spatially-dependent penalty term similar to that of Israeli and Orszag [52] and Bodony [53]. This sponge layer was applied at the inflow and outflow and appeared effective in preventing reflections from the boundaries. However, even though the sponge layer strength and extent were optimized for each case, there were still amplitude jumps upstream of the sponge layer interface in some cases. An alternative to sponge layers is the Perfectly Matched Layer (PML) as shown in Berenger [54] for electromagnetic problems. The PML surrounds the domain of interest (excluding the wall for BL stability problems, see Hagstrom et al. [55]) with an absorbing layer. The impedance of the absorption layer is perfectly matched to that of the interior domain at the interface to prevent reflections and then increases rapidly to absorb the perturbations entering the PML. Aside from using a PML, one can introduce a buffer domain that gradually parabolizes the governing equations over a short region upstream of the outflow as performed by Liu and Liu [56]. Ultimately, the most effective, efficient, and robust method for use in HNS remains uncertain and requires further investigation.

In summary, problems involving local geometric changes require stability analysis methods with increased physical modeling that still avoid the high costs of DNS. The present work introduces such a method in the form of a nonlinear harmonic Navier-Stokes solver, developed to tackle this challenge for incompressible temporally periodic and spanwise-invariant flows. The solution framework is designed to handle computer memory efficiently and independently from the mode ensemble size. The HNS equations are discretized using a generalized coordinate transform, allowing for a wide range of smooth problem geometries, while sharp wall features such as steps are modeled via an embedded boundary technique. Finally, wall-blowing and suction options are included for the introduction of arbitrary perturbations.

The structure of this report is as follows. A general form of the physical and computational domain is introduced in Sect. 2. The equations are derived and discretized in generalized coordinates in Sect. 3. Sect. 4 describes the numerical implementation tackling both the outflow treatment and the efficient treatment of memory. Grid convergence and code verification are performed in Sect. 5. Four key representative flow stability cases are used to validate the implementation against benchmark methods in Sect. 6. A conclusion on the application of the HNS framework to stability problems is given in Sect. 7.

2. Description of example problem domains

The proposed HNS framework, named DeHNSSo, is envisioned as a generalized and flexible simulation tool for a wide range of transitional flows. Wall-bounded laminar boundary layers form the key type of flows typically explored in such analyses. Due to their dominance in relevant aerodynamic applications such as unswept or swept wings, two respective transition problems are used as target cases, namely Tollmien-Schlichting waves developing in boundary layers with mild or no sweep (typically under zero or adverse pressure gradients) and stationary crossflow instabilities developing in swept boundary layers (typically under favorable pressure gradients). In this section, the physical and numerical domains are outlined wherein the HNS framework is employed. This includes the particularities of geometrical wall features.

A schematic of the four-sided numerical domain is presented in Fig. 1. It features an inflow plane, a (possibly curved) bottom wall, a top boundary, and an outflow plane. The physical semi-infinite physical domain has to be truncated to allow for a numerical assessment of the problem. This results in an imposed outflow and top boundary. To mitigate the unphysical effect of the domain truncation, an outflow buffer is implemented that prevents upstream reflections. This buffer is indicated by the shaded region in Fig. 1 and its implementation is considered in detail in Sect. 4.3. The effect of the top boundary is mitigated by ensuring a sufficiently tall domain.

Capitalizing on the ability of the HNS approach to incorporate surface wall features, DeHNSSo will be subjected to two types of wall geometry features commonly found on lifting surfaces: smooth humps and sharp forward-facing steps. These two geometric features are of scientific interest as both humps and steps naturally occur on wing surfaces due to manufacturing limitations [19,33,34,57]. Their presence has been noted to significantly modify the spatial development of disturbances responsible for boundary layer transition [23]. Nevertheless, the details of the interaction of incoming boundary layer disturbances with surface features remain largely unknown. DeHNSSo will enable future research into the vast parameter space of the effect of these features on the transition process necessary for a complete understanding of the transition process.

Sharp and smooth geometric features are dealt with in different ways within DeHNSSo. Namely, smooth features are accounted for via a domain coordinate transformation while sharp features are implemented using an Embedded Boundary Method (EBM) even though both features can be accounted for using either method. Specifically, accounting for smooth features using an embedded boundary technique means a loss of accuracy at the wall or a large increase in the number of grid points required. On the other hand, accounting for sharp features using curvilinear coordinate transformations introduces singularities in the transformations. In principle, this can be avoided by rounding sharp corners as done in Hildebrand et al. [42], but this introduces potentially large model errors. The two methods (i.e., coordinate transformations and embedded boundary method) are fundamentally different and thus introduced separately.

A smooth hump at the wall is used as a nominal example of strong local wall curvature and can be treated using a generalized domain coordinate transformation relating the Cartesian system (x, y, z) to a generalized curvilinear coordinate system (ξ, η, z). In the current implementation, the ξ-axis is fitted to the curved wall as indicated in Fig. 1 (a). The hump center location is indicated by x_m. The Virtual Leading Edge (VLE) can be seen in Fig. 1 upstream of the stability domain's inflow location present at x_0 with the flow coming from the left.

Sharp steps are treated using an embedded boundary technique as shown in Fig. 1 (b), where the no-slip condition is imposed on interior grid nodes that match the step wall coordinates. The value for x_m now corresponds to the step location. The ξ-axis is thus not conformed to the step and follows the wing surface as if no step is present. The numerical grid is arranged such that the wall and the step corner can be described exactly by the grid points. Note that the coordinate transformation and embedded boundary techniques can be combined for geometries more complex than those considered here.

3. The harmonic Navier-Stokes equations

For the present work, the Harmonic Navier-Stokes equations are derived from the generalized incompressible Navier-Stokes equations in primitive variables (i.e., in velocity-pressure formulation). Assumptions are then made on the basic flow state's spanwise dependency in conjunction with a spatial and temporal harmonic perturbation ansatz to arrive at the HNS equations.

3.1. Non-dimensionalization

All quantities in the general framework are shown in non-dimensional form. Dimensional quantities are denoted with an overbar. Similar to the PSE and DNS methodologies, the disturbance evolution is considered non-locally in HNS, and as such, global characteristic scales are used. Length quantities are normalized by the reference length $\bar{l}_{\text{ref}} = \sqrt{\bar{x}_0 \bar{\nu}_{\text{ref}} / \bar{U}_{\text{ref}}}$, defined as the Blasius length scale at the inflow (i.e., $\bar{x}_0$) of the computational domain as shown in Fig. 1. The reference kinematic viscosity is defined by $\bar{\nu}_{\text{ref}}$, and velocity quantities are normalized by the reference velocity $\bar{U}_{\text{ref}}$, taken as the external (i.e., inviscid freestream) base flow streamwise (i.e., along x) velocity at the inflow. A global Reynolds number can then be defined as $Re = \bar{l}_{\text{ref}} \bar{U}_{\text{ref}} / \bar{\nu}_{\text{ref}}$. The nondimensional wave characteristics are then calculated as $\beta = 2\pi \bar{l}_{\text{ref}} / \bar{\lambda}_z$ and $\omega = 2\pi \bar{f}\, \bar{l}_{\text{ref}} / \bar{U}_{\text{ref}}$.

3.2. The perturbed Navier-Stokes equations

The dimensionless incompressible Navier-Stokes equations read

$$\frac{\partial \mathbf{q}}{\partial t} + (\mathbf{q} \cdot \nabla)\mathbf{q} = -\nabla p + \frac{1}{Re}\nabla^2 \mathbf{q}, \tag{1a}$$

$$\nabla \cdot \mathbf{q} = 0, \tag{1b}$$

where $\mathbf{q} = [u, v, w]^T$ is the vector of instantaneous velocities and p is the instantaneous static pressure.

The HNS framework makes use of harmonic decomposition for directions of periodicity, namely the spanwise (i.e., z) and temporal (i.e., t) dimensions specifically. It is assumed that the instantaneous flow state can be decomposed into a time- and spanwise-invariant base flow and a disturbance component as

$$\mathbf{q} = \mathbf{Q} + \mathbf{q}', \tag{2}$$

and

$$p = P + p', \tag{3}$$

where $\mathbf{q}'$ and p' are periodic in z and t. The basic flow state $[\mathbf{Q}, P]^T$ is assumed to be an exact solution to the steady Navier-Stokes equations; Therefore its contribution can be subtracted from Eqs. (1) (a,b), producing the perturbation equations. The basic state is additionally assumed uniform in the third dimension (i.e., z). The perturbation equations are expressed as

$$\frac{\partial \mathbf{q}'}{\partial t} + (\mathbf{Q} \cdot \nabla)\mathbf{q}' + (\mathbf{q}' \cdot \nabla)\mathbf{Q} + (\mathbf{q}' \cdot \nabla)\mathbf{q}' = -\nabla p' + \frac{1}{Re}\nabla^2 \mathbf{q}', \tag{4a}$$

$$\nabla \cdot \mathbf{q}' = 0, \tag{4b}$$

where ∇ is the three-dimensional vector differential operator

$$\nabla = \begin{bmatrix} \frac{\partial}{\partial x} \\ \frac{\partial}{\partial y} \\ \frac{\partial}{\partial z} \end{bmatrix}. \tag{5}$$

Eqs. (4) (a,b) are solved for the velocity and pressure perturbations $\mathbf{q}'$ and p'.

3.3. The perturbation ansatz

A spatial coordinate transformation is adopted to bring the perturbation equations from the physical solution domain (x, y, z) to the generalized curvilinear numerical domain (ξ, η, z). It must be stressed that the transformation is only applied in the streamwise and wall-normal directions (i.e., x and y). To then facilitate the harmonic expansion of the equations, a vector of perturbation state variables (i.e., velocity and pressure) is introduced: $\boldsymbol{\phi}' = [\mathbf{q}', p']^T$, where $\mathbf{q}'$ and p' are defined in the transformed numerical domain: $\mathbf{q}' = \mathbf{q}'(\xi, \eta, z, t)$ and $p' = p'(\xi, \eta, z, t)$. The perturbations are then discretized using a finite sum of Fourier modes in the temporal and spanwise dimensions. The evolution of the perturbations is then described by the multiplication of an amplitude function $\hat{\boldsymbol{\phi}}(\xi, \eta)$ and an exponential wave function in z and t. The employed solution form is reminiscent of the PSE [12] or AHLNS [29] approaches, albeit the wave function does not make use of a streamwise wavenumber. No further assumptions on the importance of higher-order streamwise derivatives are made to maintain the generality of the perturbation field. The perturbations are described in the form:

$$\boldsymbol{\phi}'(\xi, \eta, z, t) = \sum_{m=-\infty}^{\infty} \sum_{n=-\infty}^{\infty} \hat{\boldsymbol{\phi}}_{m,n}(\xi, \eta) e^{\mathrm{i}(\beta_n z - \omega_m t)}, \tag{6}$$

where $\beta, \omega \in \mathcal{R}$ and $\hat{\boldsymbol{\phi}} \in \mathcal{C}$. The imaginary unit is denoted as $\mathrm{i} = \sqrt{-1}$, β is the spanwise modal wavenumber, ω is the modal angular frequency, and t is the time. The common notation (m, n) is used here to describe the relation of the wave specifications of higher harmonic modes, i.e., $\omega_m = m\omega_1$ and $\beta_n = n\beta_1$. Here ω_1 and β_1 indicate the fundamental frequency and spanwise wavenumber, respectively. In addition, the $(0, 0)$ mode has a spanwise wavenumber and angular frequency of zero. This mode specifically is referred to as the Mean Flow Distortion (MFD) and can be interpreted as the (nonlinear) modification of the base flow by the perturbations.

The ansatz of Eq. (6) is truncated to $-N \leq n \leq N$ and $-M \leq m \leq M$ to find a numerical solution. This leads to:

$$\boldsymbol{\phi}'(\xi, \eta, z, t) = \sum_{m=-M}^{M} \sum_{n=-N}^{N} \hat{\boldsymbol{\phi}}_{m,n}(\xi, \eta) e^{\mathrm{i}(\beta_n z - \omega_m t)}, \tag{7}$$

where the truncation limits of m and n are denoted by M and N, respectively. These must be chosen such that most of the perturbation energy is captured by the solution. Consequently, higher harmonics can be assumed to have a marginal effect on the instability development and can be neglected. The Fourier ansatz employed here is nearly identical to NPSE formulations in e.g., [13,21] aside from the absence of the streamwise wavenumber α. Inserting the perturbation ansatz of Eq. (7) into Eq. (4) leads to the Harmonic Navier-Stokes equations in generalized coordinates:

$$\sum_{m=-M}^{M} \sum_{n=-N}^{N} \left(\mathcal{L}_{m,n} \hat{\boldsymbol{\phi}}_{m,n} + \mathcal{M}_{m,n} \frac{\partial \hat{\boldsymbol{\phi}}_{m,n}}{\partial \xi} + \mathcal{N}_{m,n} \frac{\partial^2 \hat{\boldsymbol{\phi}}_{m,n}}{\partial \xi^2} \right) = \sum_{m=-M}^{M} \sum_{n=-N}^{N} \boldsymbol{r}_{m,n}, \tag{8}$$

where the mode-specific operators $\mathcal{L}_{m,n}$, $\mathcal{M}_{m,n}$, and $\mathcal{N}_{m,n}$ comprise the respective products with $\hat{\boldsymbol{\phi}}_{m,n}$, $\frac{\partial \hat{\boldsymbol{\phi}}_{m,n}}{\partial \xi}$, and $\frac{\partial^2 \hat{\boldsymbol{\phi}}_{m,n}}{\partial \xi^2}$. The right-hand side contains the double sum of nonlinear interactions over all considered modes. The contents and treatment of $\boldsymbol{r}_{m,n}$, i.e., the forcing of mode (m, n), are considered in more detail in Sect. 3.4.

As Herbert [13] notes, the physical field must be real and thus it must hold that

$$\boldsymbol{\phi}'_{-n,-m} = \boldsymbol{\phi}'^{\dagger}_{m,n}, \tag{9}$$

where † denotes the complex conjugate. This simple operation nearly halves the required number of calculations as shown in Fig. 2. The light-shaded area indicates the modes that can be generated from symmetry when the base flow is purely two-dimensional (i.e. $W = 0$). Then, an additional axis of symmetry is introduced in z such that:

$$\boldsymbol{\phi}'_{m,-n} = [u'_{m,n}, v'_{m,n}, -w'_{m,n}, p'_{m,n}]^T. \tag{10}$$

3.4. Harmonic balancing

The system of Eq. (8) is coupled, which complicates the development of an efficient solution algorithm. This can be simplified by employing harmonic balancing, which is based on the idea that the nonlinear interaction of two modes (i.e. their product), (ω_j, β_k) and (ω_l, β_p), results in the forcing of a third mode (ω_g, β_h) as illustrated by an example in Fig. 2. This idea originates from the NPSE methodology as shown in Herbert [13], Haynes and Reed [21], and Westerbeek [58] and is easily visualized by observing the multiplication of the respective wave functions. As an example, consider the term $-u' \frac{\partial u'}{\partial \xi}$, where u' contains the double truncated sum shown in Eq. (7). Isolating the interaction of any two modes (j, k) and (l, p), $-u' \frac{\partial u'}{\partial \xi}$ can be rewritten as:

$$\sum_{j=-M}^{M} \sum_{k=-N}^{N} \sum_{l=-M}^{M} \sum_{p=-N}^{N} -\hat{u}_{(j,k)} e^{\mathrm{i}(k\beta_1 z - j\omega_1 t)} \frac{\partial \hat{u}_{(l,p)}}{\partial \xi} e^{\mathrm{i}(p\beta_1 z - l\omega_1 t)}, \tag{11a}$$

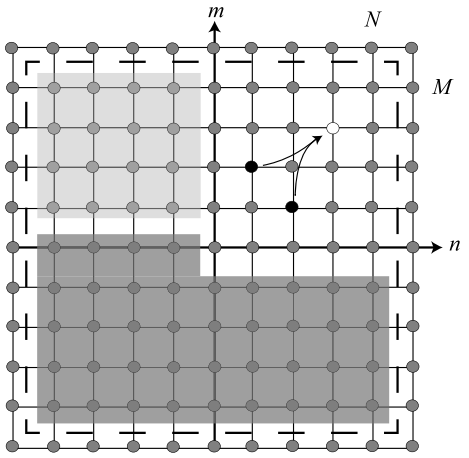

Fig. 2. Schematic of the Fourier mode space, adapted from Herbert [13]. An example of a nonlinear interaction is shown between two modes via the arrows (from black source modes to white recipient mode). The dashed outline indicates the truncated ensemble of modes (M, N) and the dark-shaded area shows modes that can be found via symmetries. The light-shaded area shows modes that can be found via symmetries in 2D flows.

$$= \sum_{j=-M}^{M} \sum_{k=-N}^{N} \sum_{l=-M}^{M} \sum_{p=-N}^{N} -\hat{u}_{(j,k)} \frac{\partial \hat{u}_{(l,p)}}{\partial \xi} e^{\mathrm{i}((k+p)\beta_1 z - (j+l)\omega_1 t)}, \tag{11b}$$

$$= \sum_{g=-M}^{M} \sum_{j=\max(g-M,-M)}^{j=\min(M+g,M)} \sum_{h=-N}^{N} \sum_{l=\max(h-N,-N)}^{l=\min(N+h,N)} -\hat{u}_{(j,k)} \frac{\partial \hat{u}_{(g-j,h-k)}}{\partial \xi} e^{(h\beta_1 z - g\omega_1 t)}, \tag{11c}$$

where in the last step interactions that exceed the spectral domain are excluded from the calculation. Thus, the mode (g, h) will be forced by every interaction of active modes (j, k) and (l, p) for which it holds that $j + l = g$ and $k + p = h$. In a given simulation, it is thus known a priori which interaction affects which mode. Consequently, only the relevant interactions are summed to find the source term that is presented on the right-hand side per mode. This results in Eq. (8) becoming at most a system of $(M + 1) \times (2N + 1)$ inhomogeneous linear equations accounting for symmetries:

$$\mathcal{L}_{m,n} \hat{\boldsymbol{\phi}}_{m,n} + \mathcal{M}_{m,n} \frac{\partial \hat{\boldsymbol{\phi}}_{m,n}}{\partial \xi} + \mathcal{N}_{m,n} \frac{\partial^2 \hat{\boldsymbol{\phi}}_{m,n}}{\partial \xi^2} = \boldsymbol{r}_{m,n}, \tag{12}$$

coupled via the nonlinear forcing terms. The matrices $\mathcal{L}$, $\mathcal{M}$, and $\mathcal{N}$ contain the information of base flow and mode characteristics. These matrices will be further scrutinized in the following sections. Therefore, the contents of $\mathcal{L}$, $\mathcal{M}$, and $\mathcal{N}$ are currently not described.

3.5. Boundary and inflow conditions

The derived system of HNS equations must be solved with appropriate boundary conditions, representing realistic physical constraints governing the evolution of the perturbations. In addition, boundary conditions can be used as convenient means for introducing forced external disturbances, for example, in receptivity studies or studies of active/passive flow control. The following gives a generalized description of boundary conditions for the domains described in Sect. 2, while details on their numerical implementation are elaborated in Sect. 4.

The harmonic Navier-Stokes equations govern the development of steady and unsteady perturbations in an otherwise steady shear base flow (e.g. a boundary layer). As such, perturbations are expected to decay in the freestream. In the discrete case, this is approximated by enforcing homogeneous Dirichlet boundary conditions for perturbation velocities at the artificial top boundary ($\eta = H$) indicated in Fig. 1. This boundary condition introduces an error as perturbations asymptotically fade into the freestream. However, for large enough H this error is as-

sumed to be negligible. This is easily verified on a case-by-case basis by performing a sensitivity study for this parameter. While this applies conceptually to all perturbation modes, particular care needs to be taken in the case of mode $\hat{\phi}_{0,0}$, i.e., the mean flow distortion. As in nonlinear PSE approaches (e.g. [13,21]), this mode is responsible for the net effect of perturbations on the base flow. Consequently, the boundary conditions should allow for this mode to have a non-zero wall-normal velocity at the top boundary. To facilitate this, the wall-normal component of the MFD is left unconstrained at the top domain. In summary, the boundary condition at the top of the domain is expressed as

$$\hat{\mathbf{q}}_{m,n}(\xi, \eta = H) = \mathbf{0} \text{ for either } m \neq 0, n \neq 0 \tag{13a}$$

$$\hat{u}_{m,n}(\xi, \eta = H) = 0 \text{ for } m = 0, n = 0 \tag{13b}$$

$$\hat{w}_{m,n}(\xi, \eta = H) = 0 \text{ for } m = 0, n = 0, \tag{13c}$$

where H denotes the domain height. Although no explicit boundary condition is presented here for the MFD wall-normal perturbation velocity, a homogeneous Neumann condition is implied via continuity:

$$\frac{\partial \hat{v}_{m,n}}{\partial \eta}(\xi, \eta = H) = 0 \text{ for } m = 0, n = 0, \tag{14}$$

since $\hat{u}_{m,n} = \hat{w}_{m,n} = 0$. Similarly, at the wall, no-slip conditions can be applied in the case of solid, non-permeable surfaces or inhomogeneous boundary conditions can be used to simulate sources of active or passive disturbance forcing such as vibrating ribbons [59], porous walls [60], sub-surface resonators [61], etc. These can be introduced as

$$\hat{\mathbf{q}}_{m,n}(\xi, \eta = 0) = \mathbf{q}^{w}_{m,n}, \tag{15}$$

where $\mathbf{q}^{w}_{m,n}$ is the wall boundary value for each individual perturbation mode. If $\mathbf{q}^{w}_{m,n} = 0$, no-slip conditions are enforced. It must be noted that pressure is only prescribed at the inflow and not at the wall or the freestream where it is solved implicitly instead. If a sharp geometrical wall feature (e.g., a step or gap) is present, the no-slip condition is additionally enforced at the wall feature's face(s). The use of embedded domain boundaries is covered in more detail in Sect. 4.

At the domain inflow, Dirichlet boundary conditions for all perturbation velocity components and pressure are applied. The inflow further presents a convenient means to introduce known disturbances, typical for classical stability analysis. For example, the local Orr-Sommerfeld eigenvalue problem can be solved at the inflow, to provide an inflow condition for one or more disturbance modes, a method commonly used in various stability analysis frameworks [12,13,21]. Not all modes need to be initiated at the inflow if their amplitudes are small, as higher harmonics and the mean flow distortion can be self-generated within the domain due to nonlinear interactions [24]. The inflow can be further used for more general types of perturbations, for example, arbitrary velocity/pressure disturbances used in non-modal stability analyses (e.g., [62,63]). A modified Dirichlet boundary condition is applied at the outflow, working in conjunction to a buffer zone implemented at the end of the domain to prevent unwanted reflections. Its implementation is considered in detail in Sect. 4.3.

4. Implementation

The implementation of the solution framework is designed with several requirements in mind. The intention is to offer a flexible and accessible method for those working in the field of stability analysis, ideally able to provide accurate results on desktop machine architectures within a reasonable time. This is greatly enabled by the efficiency and speed of the harmonic expansion, which effectively removes the need for numerical discretization in two out of four problem dimensions (i.e., z and t), as described in Sect. 4.1. This reduction of the HNS system to an essentially two-dimensional numerical problem allows for relaxing the need for high-performance computing implementations.

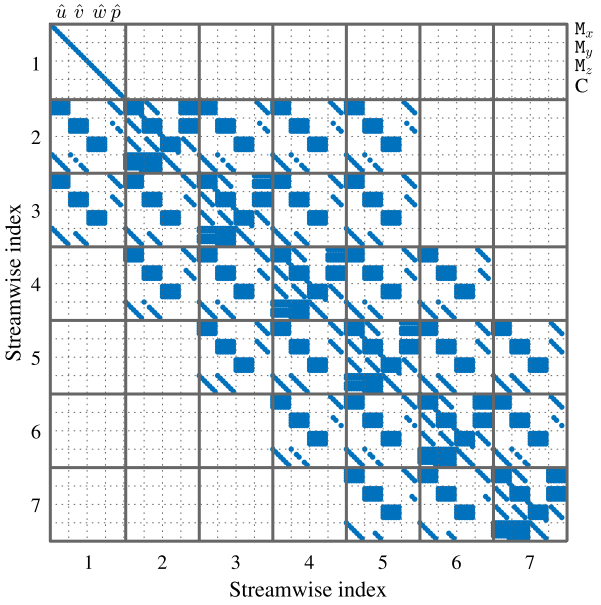

Fig. 3. Nonzero entries represented as a blue dot in the sparse banded matrix $\mathbb{M}$ with $\Gamma_\xi = \Gamma_\eta = 7$. For the first index, the shape functions $\hat{u}$, $\hat{v}$, $\hat{w}$, and $\hat{p}$ are shown that will be multiplied by the entries of that column. Likewise, $\mathtt{M}_x$, $\mathtt{M}_y$, $\mathtt{M}_z$ and the C indicate the x, y, z momentum and continuity equations respectively solved per row. (For interpretation of the colors in the figure(s), the reader is referred to the web version of this article.)

The HNS system is solved through the inversion of the equation

$$\mathbb{M}_{m,n}\hat{\boldsymbol{\phi}}_{m,n} = \mathbf{r}_{m,n} \tag{16}$$

sequentially for each mode (m, n) comprising the discretized form of Eq. (12). The state vector $\hat{\boldsymbol{\phi}}_{m,n}$ contains all perturbation velocities and pressures in the domain organized as $[\hat{u}_{1,1}, \hat{u}_{1,2} \ldots \hat{p}_{\Gamma_\xi,\Gamma_\eta}]^T$ for a specific mode, thus making it of length $4 \times \Gamma_\xi \times \Gamma_\eta$. The number of elements in the ξ-direction is described by Γ_ξ and likewise in η. The matrix $\mathbb{M}$ is a banded sparse square matrix of order $4 \times \Gamma_\xi \times \Gamma_\eta$ with a bandwidth, m_b, equal to $20 \times \Gamma_\eta$. The factor 20 originates from the fourth-order finite difference discretization scheme employed that uses a five-point stencil of order $4 \times \Gamma_\eta$ to approximate first and second-order derivatives. This band contains many zeroes as can be seen in Fig. 3. The matrix $\mathbb{M}$ is not symmetric and the band density is less than 0.5.

4.1. Discretization

The discretization of Eq. (12) is performed differently for the streamwise (i.e., along ξ) and wall-normal (i.e., along η) directions. The wall-normal derivatives are discretized using a spectral collocation method with Chebyshev polynomial bases. Spectral collocation methods are characterized by rapid convergence as a function of the number of degrees of freedom, however, come at the cost of fuller matrices. The current implementation uses the differentiation matrix suite by Weideman and Reddy [64]. Based on the theoretical collocation point distribution, the suite provides first and second-order differentiation matrices, $\mathcal{D}_1$ and $\mathcal{D}_2$ respectively. For increased resolution in the near-wall region, the distribution of collocation points is modified and clustered near the wall, following an algebraic mapping from the computational domain [0, 1] to the physical domain [0, H] as proposed by Malik [65]. The mapping uses a median collocation point to define the height η_i under which half of the collocation points reside. This distribution is stretched when a step is considered to contain a near-constant $\Delta\eta$ up to a point slightly over the step height. From that point upward, the grid becomes more coarse with the distance from the wall.

The first and second-order streamwise derivatives in the HNS equations are discretized using a fourth-order central finite-difference

scheme. This scheme becomes progressively downwind at the inflow and upwind at the outflow, as shown in Sect. 4.3. Similarly, the scheme becomes progressively upwind in the vicinity of sharp features for $\eta \leq h_{step}$ if present. The scheme is unaltered, i.e. remains centered, for $\eta > h_{step}$. More details on the treatment of these features are provided in Sect. 4.4.

4.2. Memory management and construction of the solution matrix

Matrix $\mathbb{M}_{m,n}$ from Eq. (16) is a highly sparse banded matrix. Direct sparse matrix solvers are ideal tools for this type of problem. However, while these methods are fast and robust, memory can become a bottleneck for large problems due to a phenomenon known as fill-in when factorizing a sparse matrix. Moreover, considering a given nonlinear stability problem simulation, Eq. (16) needs to be solved successively for each of the modes in the entire mode ensemble as well as repeatedly to achieve convergence of the nonlinear interaction terms (contained in $\mathbf{r}_{m,n}$). As such, accounting for symmetries, the total memory allocation necessary can reach $\Big((M+1)\times(2N+1)-N\Big)\times S$ in 3D flows ($W \neq 0$) and $(M+1)\times(N+1)\times S$ in 2D ($W = 0$) flows if $\omega_1 = 0$ or $\beta_1 = 0$, where M is the maximum number of frequency (ω) modes, N is the maximum number of spanwise wavenumber (β) modes and S is the memory size of matrix $\mathbb{M}_{m,n}$. A strategy for addressing this can be devised by first rearranging Eq. (12) to:

$$[A]\mathbf{q}_{m,n} + [B]\omega_m\mathbf{q}_{m,n} + [C]\beta_n\mathbf{q} + [D]\beta_n^2\mathbf{q}_{m,n} + [E]\frac{\partial \mathbf{q}_{m,n}}{\partial \xi} + [F]\frac{\partial^2 \mathbf{q}_{m,n}}{\partial \xi^2} = \mathbf{r}_{m,n}, \tag{17}$$

where matrices A-F contain base flow values and coefficients associated with wall-normal derivative operators only and are mode-independent (see Appendix B). Matrices A-F form the building blocks for the left-hand side matrix $\mathbb{M}_{m,n}$. Using Eq. (17), the left-hand side of Eq. (16) can be created at every iteration using

$$\mathbb{M}_{m,n} = \mathbb{M}_1 + \mathbb{M}_2\omega_m + \mathbb{M}_3\beta_n + \mathbb{M}_4\beta_n^2, \tag{18}$$

where the streamwise derivatives are approximated via finite-difference operators contained in $\mathbb{M}_1$. This allows common and mode-invariant matrices $\mathbb{M}_1$ to $\mathbb{M}_4$ to be recycled during the simulation. In fact, sparse matrices $\mathbb{M}_1$ to $\mathbb{M}_4$ need only to be constructed once before the beginning of the simulation and can be accessed in parallel by separate computational cores, each evaluating different modes. In summary, with the described procedure, the total memory used to store the left-hand side matrices for a given simulation is significantly reduced to S, (i.e., the size of $\mathbb{M}_1$) plus the overhead associated with storing the three additional highly-sparse matrices ($\mathbb{M}_2 - \mathbb{M}_4$). In addition, due to the avoidance of constructing the lengthy matrix $\mathbb{M}_{m,n}$ repeatedly, gains in computational time are achieved. The generalized construction of the matrices $\mathbb{M}_1$ to $\mathbb{M}_4$ can be found in Appendix C. The memory required to solve Eq. (16) scales with the numerical grid only. Specifically, it was found that the memory requirements saving $\mathbb{M}$ and solving the problem both scale linearly with Γ_ξ and quadratically with Γ_η.

4.3. Outflow treatment

A considerable challenge in incompressible NS solution frameworks is the treatment of spurious reflections from numerical domain boundaries. This is a direct result of the introduction of an outflow boundary when modeling the semi-infinite domain as a finite domain [35]. Streett and Macaraeg [66] note that the ellipticity in the incompressible Navier-Stokes equations allows for the upstream travel of information which arises primarily from the viscous terms and the pressure field term. Joslin [67] notes that the interaction of local velocity perturbations with the pressure boundary causes a pressure pulse that travels upstream at infinite speed for incompressible simulations. Consequently, neither Dirichlet nor Neumann boundary conditions can be imposed directly at the outflow.

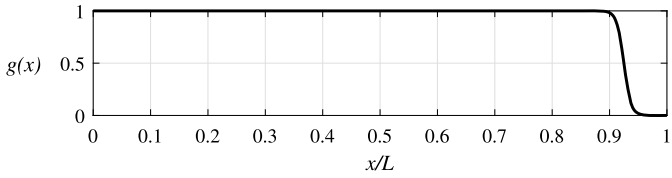

Fig. 4. Streamwise dependency of the buffer function, $g(x)$, starting at $x_b = 85\%$ of the domain for a normalized domain length $x/L = [0, 1]$. The buffer has no effect for a value of 1 and maximum effect at the end of the domain with a value of $\approx 6 \times 10^{-6}$ for $\kappa = 6$.

To avoid this unphysical behavior in the present implementation, streamwise and spanwise perturbation velocities are damped within a buffer region located upstream of the outflow (see Fig. 1). This buffer significantly reduces the strength of reflections originating from the outflow. Damping is performed by multiplying all terms by a buffer function $G(x)$ and then adding its reciprocal $(1 - G(x))$ to the diagonal terms of matrix $\mathbb{M}$ corresponding to the streamwise and spanwise perturbation components. This adapts the equations to ensure the streamwise and spanwise perturbation components become smoothly negligible. Mass continuity ensures that the wall-normal velocity and pressure perturbation components are attenuated in a similar fashion while not over-constraining the equations. The attenuation function is adapted from Joslin [67] as:

$$g(x) = \frac{1}{2}\left(1 + \tanh\left(\kappa\left[1 - 2\frac{x - x_b}{x_e - x_b}\right]\right)\right), \tag{19}$$

where x_b and x_e refer to the starting and ending location of the buffer respectively and κ is a stretching factor, equal to 6 for the cases presented here. This function is scaled so that no discontinuity exists in the buffer function $G(x)$ at $x = x_b$. The buffer formulation then reads:

$$G(x) = \begin{cases} 1 & x < x_b \\ 1 - \frac{g(x)}{g(x_b)} & x \geq x_b \end{cases} \tag{20a}$$

where $g(x)$ is used to distinguish between the attenuation function shape and the buffer formulation $G(x)$. For cases presented here, this method has been effective in preventing outflow boundary interactions in the domain of interest.

Fig. 4 shows the streamwise dependency of the attenuation function. In addition to directly attenuating the disturbance velocities, the buffer is also applied to the nonlinear terms. This is performed via a direct multiplication with the local buffer function value. This ensures that the right-hand side of Eq. (16) is near-zero at the outflow.

4.4. Embedded boundary method

In the present implementation, sharp geometric wall features (e.g., a step) are introduced in a way similar to the immersed boundary method commonly used in DNS applications (see e.g., Meyer et al. [68] and Örley et al. [69]). As such, the grid domain is not conformed to the step, but the interior nodes are adjusted to the step wall to ensure that a collocation point coincides exactly with the step corner. The left-hand side matrix $\mathbb{M}$ can now be manipulated such that the proper boundary conditions are enforced. More specifically, no-slip and impermeability conditions are imposed at points that coincide with the step wall while perturbation pressures are solved implicitly. Grid points that exist underneath the step surface do not enter the finite difference stencil as the scheme is adjusted to become progressively upwind in the proximity of the step. This shift toward a more upwind stencil is only performed for grid points below the step corner. Above the step, the stencil is unaffected, and a fourth-order central finite-difference stencil is maintained

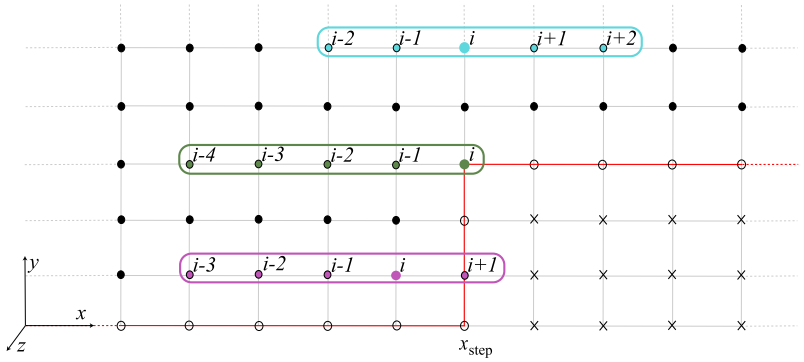

Fig. 5. Three finite-difference stencils color-coded for several streamwise stations i around the step with dots, circles, and crosses representing internal, surface, and sub-surface grid points respectively. The red line represents the solid wall.

as is visualized in Fig. 5. The wall-normal derivative operators are unaffected by the presence of a step.

4.5. Iterative convergence of the nonlinear terms

One of the distinguishing features of the presented HNS framework is its ability to treat nonlinear stability problems efficiently. In classical NPSE approaches, the nonlinear terms can be converged at every streamwise station separately (see [12,13,21]). This is made possible by the parabolization of the equations allowing them to be solved in a marching fashion. In HNS, the entire flow field must be considered per iteration. The nonlinear terms thus have to be converged from an initial guess, which is typically the solution to the linear problem. Based on this approach, Rigas et al. [45] solved the coupled nonlinear system using an iterative Newton algorithm. This requires the nonlinear terms to be maintained on the left-hand side of Eq. (8) and the full Jacobian to be calculated for the nonlinear system. Although proven effective for the studied cases, its high computational cost is noteworthy. Specifically, due to the need to solve for the entire modal ensemble simultaneously, the problem scales rapidly with the number of modes considered.

An iterative approach is adopted in this work, which is independent of the total number of modes considered. The nonlinear terms are maintained as a lagged source term on the right-hand side (see Eq. (12)) and can be iteratively constructed for each mode. This is analogous to the treatment of nonlinear terms in the NPSE, albeit considering the entire flow field. Generally, lagged approaches are less robust than, e.g., an iterative Newton algorithm. To overcome this shortcoming, an amplitude ramping procedure is employed.

4.5.1. Amplitude ramping

A key challenge in the iterative construction of the nonlinear terms in Eq. (12) is the appearance of nonphysical and diverging solutions. Specifically, a non-linear simulation needs to be initialized with at least one perturbation mode (e.g. the fundamental mode), typically extracted from a linear eigenvalue solution. However, for particular types of instabilities, linear stability analysis can lead to unrealistically large amplitudes in the domain. In crossflow-dominated flows especially, disturbance amplitudes several times greater than the base flow freestream velocity value can be reached purely based on linear growth. Fig. 6 provides an example thereof for a stationary CFI mode in a swept-wing boundary layer. While the nonlinearly developing fundamental mode reaches amplitude saturation (i.e., $u'_{max} \approx 0.3$, see [21,70]), the linear solution (initialized with the same inflow amplitude) would approximate or surpass a value of 1 within the considered domain. Initializing a nonlinear simulation with this linear solution would force the second, third, etc. harmonics to reach amplitudes of $O(u'_{max})^2$, $O(u'_{max})^3$, etc. This causes a divergence of the nonlinear terms and an eventual blow-up of the simulation. Herein lies the challenge for nonlinear convergence of HNS, as the calculation of nonlinear terms that enforce

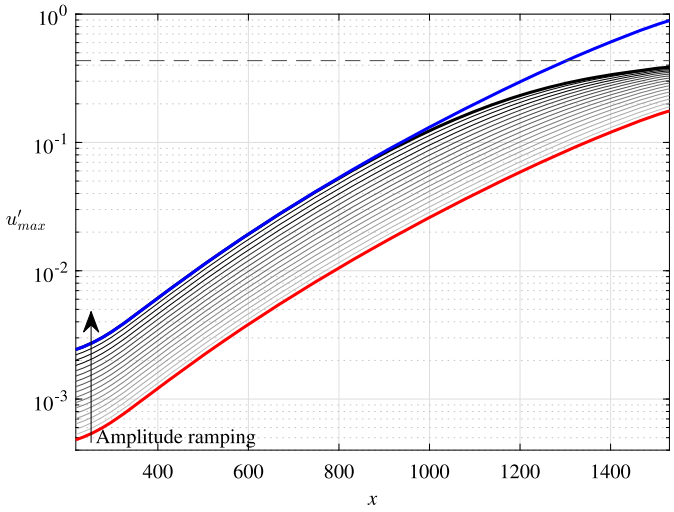

Fig. 6. Initial (light) to final (dark) stationary crossflow instability amplitude development (based on maximum streamwise perturbation velocity) of the fundamental mode in a swept-wing boundary layer with $N = 5$ during amplitude ramping. Higher harmonics are not shown. Red and blue lines represent linear amplitude developments corresponding to the highest and lowest inflow amplitude respectively. The dashed line indicates the approximate amplitude limit over which non-physical solutions would occur in the current domain.

amplitude saturation relies on the presence of mode harmonics, most notably the mean-flow distortion [71].

In the present implementation, this problem is overcome by reducing the inflow amplitude for the linear simulation used to provide the initial guess for the HNS solution. This amplitude is found a posteriori such that the maximum amplitude does not exceed a pre-determined threshold (AMAX) within the considered domain. Since the simulation was linear, it can be scaled to the desired inflow amplitude directly. However, the proper amplitude threshold is difficult to predict as it depends on the significance of nonlinear dynamics. In practice, an effective threshold is easily found by trial and error, and setting it too low can at most result in slightly longer computation times. In the present work, the threshold is set to 20% of the reference velocity for all cases. The nonlinear continuation approach is then started; The inflow amplitude is slowly increased until the desired inflow amplitude is reached. The amplitude ramping is done using two modes and the MFD such that nonlinear divergence is prevented. For the test cases presented here, using the second harmonic and the MFD was sufficient to achieve this. The expansion of the spectral ensemble by the generation of new harmonics is performed under two conditions: If there is only one active mode (e.g. the fundamental mode), the second harmonic and the mean flow distortion are introduced. If 2 modes are already active, higher harmonics (e.g. $n > 2$) are only introduced in sequence when the goal

amplitude is reached and each new harmonic is converged before a higher harmonic is introduced.

The convergence criterion for a mode (m,n) can be calculated as:

$$\sigma^k_{m,n} = \frac{1}{\Gamma_x}\sum_{i=1}^{\Gamma_x}\left(\frac{\left|A^k_{i,\max} - A^{k-1}_{i,\max}\right|}{A^k_{i,\max}}\right)_{m,n} \tag{21}$$

where the amplitude measure, A, is the peak amplitude of the streamwise perturbation velocity u' at a streamwise index i and k is the iteration counter. The convergence criterion σ is evaluated for all harmonics in z and t separately and none should exceed the criterion before proceeding. A relative amplitude convergence criterion of 10^{-6}(in units of U_{ref}) is used for the results presented here. An exception is made for the higher harmonics whose maximum amplitude can be of the order of 10^{-10} such that this criterion reaches the order of machine accuracy (10^{-16}). An absolute limit of 10^{-14} is therefore applied to the numerator of Eq. (21), below which the mode is always assumed to have converged.

4.5.2. Continuation procedure

Considering the previously described amplitude ramping approach, in the first iteration the fundamental mode amplitude is computed linearly. This result is used to calculate a nonlinear forcing term for the MFD and the second harmonic. This allows for the calculation of a nonlinear forcing term of the fundamental mode. During this continuation loop, new modes are introduced if their forcing exceeds the pre-determined case-dependent threshold.

The iterative scheme can be shortly summarized as

$$\mathbb{M}_{(m,n)}(A^{k=0}_{(m,n)}) = 0, \quad \mathbf{f}^{k=1}_{(m,n)} = \mathbb{NLT}(\hat{\boldsymbol{\phi}}^{k=0}_{(m,n)}), \tag{22a}$$

$$\mathbb{M}_{(m,n)}(A^{k+1}_{(m,n)}) = \mathbf{f}^{k}_{(m,n)}, \quad \mathbf{f}^{k+1}_{(m,n)} = \mathbb{NLT}(\hat{\boldsymbol{\phi}}^{k}_{(m,n)}), \tag{22b}$$

where $\mathbb{M}$ is the linear HNS operator, written here as a function of the initial amplitude given to the fundamental mode(s). The operator $\mathbb{NLT}$ comprises the nonlinear terms that define $\mathbf{f}^{k+1}$ based on an intermediate solution, $\hat{\boldsymbol{\phi}}^k$, which should be converged before proceeding to greater inflow amplitudes. For sufficiently small initial amplitude increment, γ, $\mathbf{f}^{k-1} \approx \mathbf{f}^k$ and the problem does not diverge. However, a small γ is associated with large computation times. For simulations presented here, $\gamma = 1.1$.

The forcing term shown in Eq. (22) (b) is linearly extrapolated to aid in the numerical stability and speed of the iteration procedure from $k = 3$ onward. This extrapolation can be described as:

$$\mathbf{f}^k_{(m,n,i)} = \mathbf{f}^{k-1}_{(m,n,i)} + \frac{\mathbf{f}^{k-1}_{(m,n,i)} - \mathbf{f}^{k-2}_{(m,n,i)}}{A^{k-1} - A^{k-2}}(A^k - A^{k-1}), \tag{23}$$

for all active modes in both the current and previous iterations. In the strongly nonlinear saturated regimes within the computational domain, $\mathbf{f}^k \approx \mathbf{f}^{k-1}$ since $\mathbf{f}^{k-2} \approx \mathbf{f}^{k-1}$. Consequently, the effect is largest for lower amplitudes where the behavior is linear in amplitude. The procedure for solving the HNS iteratively is presented as pseudo-code in Algorithm 1.

Algorithm 1 HNS Solver Pseudo Code.

procedure FIND A LINEAR INFLOW AMPLITUDE
Inflow Eigenvalue Problem:
    Impose inflow condition (LST, LOAD, or ZERO)
    Present the LST solution on the right-hand side for the first stage
Initial Linear Estimate:
    Solve the linear problem
    Find $A_{\max}$
    Reduce the inflow amplitude A_0 to ensure $A_{\max}$ = AMAX

procedure CONVERGE THE NONLINEAR PROBLEM
while $A_0 \leq A_{\text{goal}}$
while $\epsilon >$ nonlinear convergence threshold
Calculate Nonlinear Terms:
    Compute nonlinear terms based on the latest iteration
Solve Nonlinear Problem:
    Solve HNS
Introduce Harmonics:
if Number of active modes is less than 2 **or** goal initial amplitude is reached
    Introduce new modes
end if
Perform Convergence Check:
    Calculate the change in normalized amplitude evolution, ϵ
end while
    Increase inflow amplitude as $A_0^{k+1} = \gamma * A_0^k$
    Extrapolate forcing term
end while

    CLOSE;

5. Verification

Before the developed HNS framework will be compared to benchmark methods such as NPSE, AHLNS, and DNS, it is desirable to establish the dependence of the outcomes on the numerical and discretization parameters. In this section, the HNS implementation is verified by assessing the observed convergence rate and comparing it to the expected convergence rate based on the formal discretization schemes used in the current implementation.

As a verification test case, the nonlinear development of TS waves in the Blasius boundary layer ($M = 5$) was used, essentially replicating the conditions simulated by Herbert in his seminal PSE report [13]. The case will be described in detail in Sect. 6.1. For details on nondimensionalization, the reader is referred to Sect. 3.1. In short, the flow is described by a constant external velocity $\bar{U} = 10$ m/s. The Blasius length at the inflow ($\bar{\delta}_0 = 6.075\times10^{-4}$ m) serves as the reference length. A global Reynolds number $Re = \frac{\bar{\delta}_0 \bar{U}_e}{\bar{\nu}} = 400$ is then defined using a kinematic viscosity of $\bar{\nu} = 1.5188\times10^{-5}$ m^2/s. The primary mode with fundamental frequency is $\omega_1 = 0.0344$ is introduced at the domain inflow as the solution to the local eigenvalue problem on which an initial amplitude of $A_0 = 0.0025\sqrt{2}$ is imposed. All higher harmonics are set to 0 at the inflow and are generated nonlinearly in the interior domain. The natural forcing of the higher harmonics ensures a constant phase relation to the fundamental mode which is introduced with an arbitrary phase. Aside from this phase shift, the downstream results are confirmed to not be affected by the phase of the inflow condition.

The results are subjected to variations in the streamwise discretization (for constant $\Gamma_\eta = 100$) and the number of Chebyshev collocation points in the wall-normal direction (for constant $\Gamma_{\bar{\xi}} = 2674$). The streamwise discretization is equidistant while the wall-normal discretization is clustered near the wall as described in Sect. 4.1. Other important parameters can affect the result through their influence on the grid, such as the median collocation point, y_i, and domain size parameters, H, L, and x_b. Preliminary convergence tests were performed (not shown here for brevity) for these parameters. Consequently, they are not varied in the convergence study and their value will be constant for all simulations: $H = 99$, $y_i/H = 0.05$, $L = 2.625\times10^3$, and $x_b/L = 0.85$. The convergence threshold, $\sigma^k_{m,n}$, was lowered significantly here to 10^{-8} to ensure its effect on the outcomes is orders of magnitude smaller than the discretization error.

Two evaluation metrics are used to evaluate the grid convergence. Firstly, an integral measure of perturbation kinetic energy E over the total physically relevant domain (x_0 x_b), between the inflow and buffer starting location respectively, is used. This can be calculated as:

$$E = \int_{x_0}^{x_b}\int_0^H \frac{1}{2}\left(|u'|^2 + |v'|^2 + |w'|^2\right) dy\, dx. \tag{24}$$

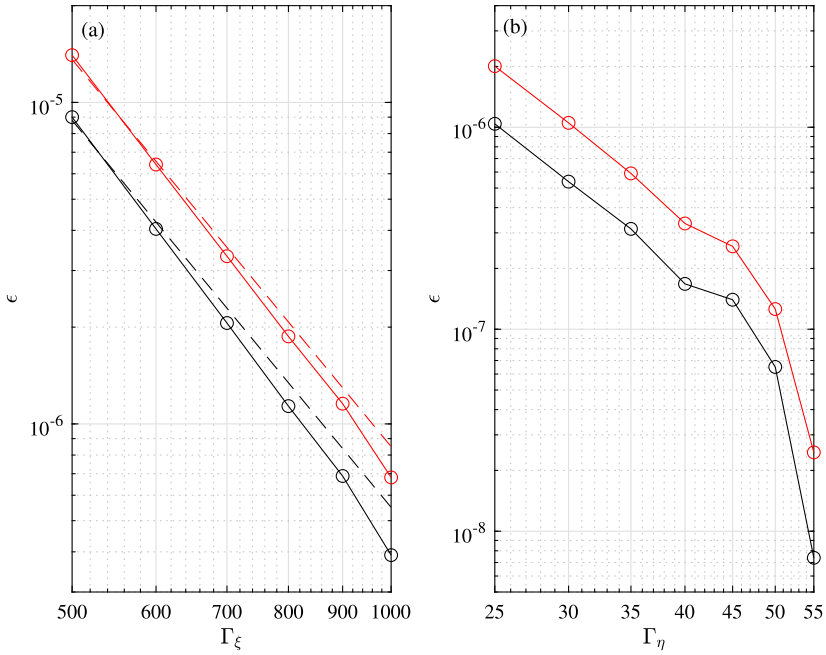

Fig. 7. Perturbation kinetic energy difference (ϵ) with respect to the most refined simulation as a function of Γ_x for constant $\Gamma_\eta = 100$ (a) and Γ_η for constant $\Gamma_\xi = 2674$ (b) based on total perturbation energy (black) and locally at $x = 1700$ (red). Markers represent simulation results. The expected convergence is indicated by the dashed line.

This integral perturbation kinetic energy measure is calculated as the modal total perturbation energy, i.e. the sum of all modes, and shown in Fig. 7. In addition, a local measure of perturbation kinetic energy is evaluated locally at $x = 1700$:

$$E = \int_0^H \frac{1}{2}\left(|u'|^2 + |v'|^2 + |w'|^2\right) dy|_{x=1700}. \tag{25}$$

The results are expected to converge with the order of $(\Delta\xi)^4$ as indicated by the dashed line in Fig. 7 (a). The absolute difference ϵ is introduced to describe the difference in integrated nondimensional perturbation kinetic energy E between the current case and the finest case. The convergence behavior is as expected. Concerning the wall-normal discretization, the shape functions for this case feature no singularities in the domain. Boyd [72] states that the Chebyshev series of functions without singularities can be expected to have supergeometric convergence. For such functions, the exponential index of convergence should increase with the number of Chebyshev polynomials included as is seen in Fig. 7 (b). Similar convergence trends are observed for all considered cases in the present work and results are available upon request to the authors.

6. Validation

The HNS framework described above was used to analyze four classical and practically relevant boundary layer stability cases. The first case considers the nonlinear growth of Tollmien-Schlichting waves in a Blasius boundary layer, outlined in Sect. 6.1. In the second example (Sect. 6.2), the nonlinear development of stationary Crossflow Instabilities (CFI) in a swept-wing boundary layer is considered. This case requires the amplitude ramping procedure described in Sect. 4.5.1. Lastly, two modifications of the latter swept-wing scenario were considered to demonstrate the implementations of smooth and sharp wall features as explained in Sect. 2. The addition of non-homogeneous wall boundary conditions (here blowing and suction) are used to trigger the CFI mode in the final case. For each case, benchmark solutions from well-established stability frameworks and/or DNS are used for validation. The four presented reference cases collectively call all terms of the Harmonic Navier-Stokes equations (i.e. frequency and spanwise wavenumber terms) and make use of all features of the implementation (i.e., generalized coordinates, embedded boundary method, amplitude ramping, outflow buffer and non-homogeneous boundary conditions). This ensures that the current implementation is thoroughly tested. The individual cases are explained in more detail in their respective sections (i.e. Sects. 6.1 - 6.4.)

It is stressed here that the results presented in this section were calculated on a grid refinement that far exceeded the minimum requirements for sufficient accuracy. It was ensured that the chosen grid did not affect the results. As was shown in Fig. 7, results converge rapidly, and coarser grids still provide accurate solutions ($\epsilon \approx 10^{-5}$). Appendix A additionally shows the computational requirements needed to solve the HNS on grids with medium refinement. The use of a coarser grid leads to computation times orders of magnitude lower than the refined simulations with a negligible loss of accuracy of the result.

6.1. Nonlinear development of two-dimensional Tollmien-Schlichting waves

The first case considering the nonlinear growth of Tollmien-Schlichting waves in a Blasius boundary layer has been studied in detail before in e.g. Bertolotti et al. [12], Chang et al. [73] and Herbert [74]. In short, the case is defined by a constant external velocity $\bar{U}_{ref} = \bar{U}_e(x) = 10$ m/s (i.e., zero pressure gradient) and a flat plate geometry. The global Reynolds number $Re = \frac{\bar{\delta}_0 \bar{U}_e}{\bar{\nu}} = 400$ is defined by the Blasius length scale at the inflow, $\bar{\delta}_0 = 6.075 \times 10^{-4}$ m, and the kinematic viscosity $\bar{\nu} = 1.5188$ m^2/s. The primary TS wave mode (1,0) is enforced at the inflow as a solution to the local eigenvalue stability problem. The primary mode is characterized by $\omega_1 = 0.0344 = \frac{2\pi \bar{f} \bar{\delta}_0}{\bar{U}_0}$ where $\bar{f} = 90.6$ Hz.

The basic flow state used for this problem is the steady solution to the incompressible boundary layer equations initiated from the Falkner Skan Cooke (FSC) solution at the inflow. The equations were subject to Neumann boundary conditions for the velocity at the freestream and Dirichlet boundary conditions for pressure. No slip and impermeability conditions are imposed at the wall. For comparison and validation of the HNS results, the amplitude evolution of the first five harmonics

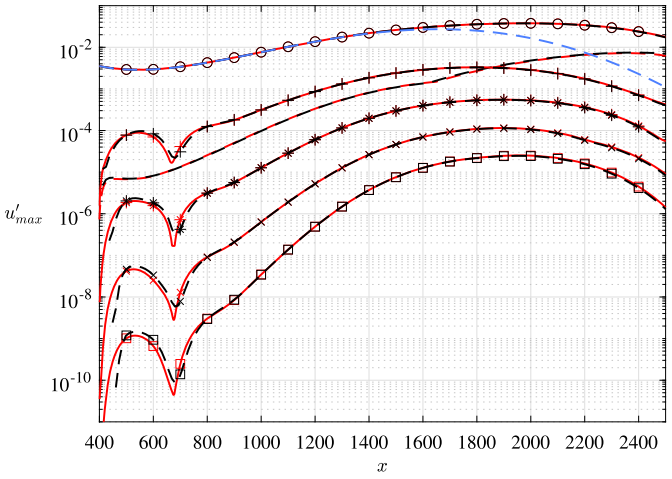

Fig. 8. Amplitude evolution of TS waves in a Blasius boundary layer at $Re_0 = 400$ and $\omega_1 = 0.0344$ showing modes (1,0) (o), (2,0) (+), (3,0) (*), (4,0) (x) and (5,0) (□) and mean flow distortion (0,0) (no marker) as calculated by NPSE (dashed black) and the current HNS (red solid lines). The linear amplitude evolution of mode (1,0) is indicated by the blue dashed line.

and the mean-flow distortion are calculated using an in-house cross-validated NPSE solver used in Westerbeek [58], Zoppini et al. [75], and Casacuberta et al. [33]. The primary (1,0) mode was introduced at the inflow with a peak streamwise perturbation velocity of $A_0 = 0.0025\sqrt{2}$, corresponding to the target test case in Bertolotti et al. [12]. All other modes are set to zero at the inflow and they are generated in the domain through nonlinear interactions.

For HNS simulations, a rectangular Cartesian grid was discretized with 2674 equidistant grid points along x, resulting in approximately 65 grid points per wavelength for the fundamental mode and 13 grid points per wavelength for the highest harmonic. In the y direction, the grid features 100 Chebyshev collocation points. The median collocation point $y_i = 4.95$. For the reference NPSE run, the domain was discretized in 200 streamwise locations with the wall-normal discretization identical to that of HNS. The streamwise extent of the domain for both NPSE and HNS was from $x = 400$ to $x = 2487$. The HNS domain was artificially extended to account for the addition of the buffer region, ranging from $x = 2487$ to the outflow at $x = 2854$. For the present case setup and considered domain extent, the primary TS wave mode (1,0) essentially convects through both branches I and II of the neutral stability curve. As such, a natural decay of the primary mode can be expected downstream of $x \approx 2000$. Consequently, nonlinear terms did not need to be damped upstream of the buffer region as the amplitudes decayed significantly between the peak value around $x = 2000$ and the start of the buffer region. Furthermore, the linear evolution of the primary mode from $A_0 = 0.0025\sqrt{2}$ does not reach unphysical amplitudes, making the suppression of nonlinear terms by means of amplitude ramping unnecessary for this case. The NPSE methodology was significantly faster for this problem; On a desktop machine (see system A in Appendix A) it took 1.5 hours (= 12 CPU core hours) to solve the nonlinear problem with NPSE while DeHNSSo required nearly 12 hours (= 96 CPU core hours).

Fig. 8 shows a good agreement between NPSE and HNS. This is expected given that the difference between the two sets of equations lies in the second-order streamwise derivative terms which are very small in this case. Only minor differences are observed in the results present in the higher harmonics near the inflow, possibly related to the sequential introduction of harmonics in the NPSE procedure. However, this does not affect the downstream result as the initial amplitudes are small, resulting in a largely linearly governed perturbation development at the inflow for the primary mode (1,0). The higher harmonics rapidly converge shortly downstream of the inflow (at around $x = 800$) where a good match with HNS is seen. A strong decline of the higher harmonics' amplitudes can be seen around $x = 700$. This behavior is not directly visible in earlier works due to the linear scaling present in the y axis, see Bertolotti et al. [12], Herbert [13], or it is less pronounced as shown in Chang et al. [73]. In the latter, it is likely a result of phase differences between the various modes. The evolution of the mean-flow distortion matches closely between the two simulations as can be seen from the kink in the amplitude curve at $x \approx 1700$. This kink is the result of tracing the maximum amplitude of the mode, which for the MFD switches abruptly between two local maxima at $x = 1700$ [12,13,73].

6.2. Nonlinear development of stationary crossflow instabilities

Next, the nonlinear growth of stationary CFI is simulated for the flow case examined in Casacuberta et al. [31], specifically their case A. The steady-state DNS results are used as the base flow to the stability problem. The case considers a flat plate geometry with an externally imposed favorable pressure gradient, obtained from wind tunnel experiments by Rius-Vidales and Kotsonis [34]. The resulting external inviscid velocity depends on the streamwise coordinate and can be approximated by the following polynomial fit:

$$U_e(x) = 1.8574 + 0.5303\ln(x) + 0.1752\ln^2(x) + 0.0377\ln^3(x) + 0.0023\ln^4(x), \tag{26}$$

normal to the leading edge, while the external spanwise velocity $W_e = -1.24$ is constant over the domain. The simulation domain starts at 5% of the wing chord length (corresponding to $x = 220\bar{\delta}_0$), where $\bar{\delta}_0 = 2.14 \times 10^{-4}$ m. This results in a global Reynolds number $Re = \bar{\delta}_0 \bar{U}_0 / \bar{\nu} = 220$ for $\bar{\nu} = 1.47 \times 10^{-5}$ m^2/s and $\bar{U}_0 = 15.1$ m/s.

The domain ranges from $x = 220$ to $x = 1560$ and has a domain height $H = 89$. It is discretized by 1272 equidistant grid points in x, resulting in approximately 35 grid points per wavelength for the fundamental mode and 8 grid points per wavelength for the highest harmonic. The grid is defined on 100 collocation points in y clustered near the wall with the median collocation point present at $y_i = 4.5$. The outflow buffer starts 15% upstream of the outflow boundary from $x = 1360$. The nonlinear forcing terms are instead suppressed from 20% upstream of the outflow.

The primary stationary CFI mode (0,1) is characterized by a spanwise wavenumber $\beta_1 = 0.18$ corresponding to a spanwise wavelength of 7.5 mm and $\omega_1 = 0$. The enforced perturbation shape at the inflow, $\hat{\phi}$, is found by solving the local linear stability eigenvalue problem. A peak streamwise perturbation amplitude of $A_0 = 3.5 \times 10^{-3}$ is then imposed on the solution. All higher harmonic modes are set to zero at the inflow and rise naturally from nonlinear interactions downstream.

A linear calculation of the development of the primary mode (0,1) results in large amplitudes for this case as explained in Sect. 4.5. The nonlinear iteration procedure diverges rapidly if this initial linear guess is used directly. Hence, amplitude ramping was required for this case. The initial amplitude was reduced to $A_0 = 2.6 \times 10^{-4}$, a factor 13.3 lower than the goal amplitude. The inflow amplitude was then gradually increased by $\gamma = 10\%$ per iteration. Consequently, 27 iterations were required to converge the nonlinear terms.

The results are compared to two benchmark simulation methods: DNS and NPSE. Both methods were found to be in good agreement in earlier work (Casacuberta et al. [33]). DNS simulations were performed using the conservative finite volume solver INCA (see Hickel and Adams [76] and Hickel et al. [77]). Herein, the domain was discretized in 6760 cells in the streamwise direction. In the wall-normal direction, the domain is discretized in 576 cells. Lastly, 72 cells were present in the spanwise direction. INCA features a fifth-order upwind scheme for the convective terms while viscous terms are discretized using a second-order central difference scheme. It took a total of 8.8 days to find the solution using 2000 CPUs in parallel for a total of approximately 500.000 CPU core hours. The NPSE simulations were performed

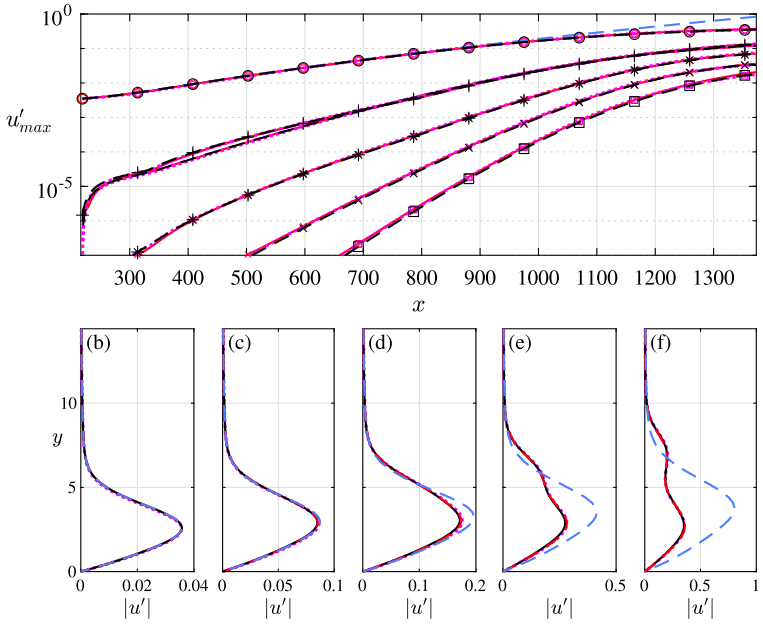

Fig. 9. Amplitude development (a) of the first (o), second(+), third(*), fourth(x) and fifth (□) crossflow instability modes and the mean-flow distortion (no marker) as calculated by HNS (black dashed), DNS (magenta dotted) and NPSE (red solid lines). The linear solution is indicated by the dashed blue line. The streamwise perturbation shape is shown for $x =$ (b) 651, (c) 829, (d) 1009, (e) 1189, and (f) 1359.

using the same basic state calculated in INCA. The flow was interpolated on the numerical domain discretized in 80 Chebyshev polynomials in the wall-normal direction and 500 streamwise stations. NPSE found the solution in approximately 3 hours (24 CPU core hours), whereas DeHNSSo took nearly 4 days (768 CPU core hours) on a desktop machine (see system A in Appendix A).

Using both the HNS and NPSE, five stationary CFI modes ($M = 0, N = 5$) and the mean flow distortion mode (0,0) were computed and are shown alongside DNS results in Fig. 9. Furthermore, the absolute perturbation shapes shown in Fig. 9 (b-f) demonstrate a close match between all methods throughout the domain. The secondary lobe present in the shape functions displayed in 9 (f) has a nonlinear origin and is captured by all three methods that accounted for nonlinear interactions.

6.3. Linear development of stationary crossflow instability over a hump

Smooth surface protuberances (i.e., humps) are unavoidable on wing surfaces [28]. The presence of such humps is known to lead to a local acceleration of the base flow [78], which in turn affects the stability of the boundary layer. Moreover, classical stability methods have repeatedly been shown to be unreliable in such cases, see Franco et al. [29], Cooke et al. [30], and Westerbeek et al. [24]. Here, the stability of a three-dimensional boundary layer featuring a hump is considered to validate the implementation of the generalized transformation approach in the present HNS framework. The examined case was previously studied in Westerbeek et al. [24], there denoted case B1, to which the reader is referred for a more detailed (nonlinear) analysis.

The flow setup is defined by the reference Blasius length at the inflow, $\bar{\delta}_0 = 2.14 \times 10^{-4}$ m, and reference velocity $\bar{U}_0 = 15.1$ m/s. This results in $Re = 220$. The domain ranges from $x = 220$ to $x = 2165$ and has a height $H = 89$. The external flow is equal to the previous validation case of Sect. 6.2. The external velocity normal to the leading edge thus follows Eq. (26) and the spanwise velocity is constant over the domain, namely $W_e = -1.24$. The hump is described as a smooth surface protuberance with a width b of 39.9 $\bar{\delta}_0$ and a height h of 2.5 $\bar{\delta}_0$. The wall is described by

$$y_{\text{wall}}(x) = h \exp\left[-\left(\frac{x_m - x}{b}\right)^2\right], \tag{27}$$

with the hump center located at $x_m = 859$. The buffer starts from $x = 1873$.

Due to the presence of the hump, the boundary layer equations cannot reliably predict the evolution of the base flow. As such, the base flow solution was found using the finite-element solver COMSOL [79]. The setup featured second-order elements for velocities and first-order elements for pressure. The grid was clustered near the wall using 115 elements in the wall-normal direction and additionally refined around the hump in the streamwise direction, in which 945 elements are present. Two elements are present in the spanwise direction in which periodic boundary conditions were imposed. A top pressure condition was imposed as was done for the swept flat plate case in Sect. 6.2 (see Casacuberta et al. [31]). At the top boundary, velocities were subjected to a homogeneous boundary condition for the second-order derivatives. At the inflow, a Falkner Skan Cooke boundary layer profile was used, corresponding to the local pressure gradient. No-slip conditions were imposed on the (curved) wall and a static pressure equal to the local top boundary pressure was imposed at the outflow. The static pressure at the top boundary follows directly from the external velocity presented earlier in Eq. (26). As the purpose of this case was merely to validate the implementation of the generalized transformation approach, the hump was made shallow to avoid flow separation. The base flow solution was interpolated onto the numerical grid via COMSOL for Matlab which uses COMSOL's built-in interpolation algorithm. This interpolation has the accuracy of the used elements (i.e., second-order for velocities and first-order for pressures).

The HNS domain is discretized with 2000 grid points in the streamwise direction. The wall-normal direction is represented by 100 collocation points with the median collocation point at a constant distance of $4.45\bar{\delta}_0$ from the wall. This discretization results in approximately 48 grid points per wavelength. The grid was conformed to the hump as shown in Sect. 2, while the η coordinate remains parallel to the global y-axis for HNS computations. The grid can be seen in Fig. 11.

A limited selection of modeling tools that can solve this problem nonlinearly are available. Hence, the specific validation is performed linearly. Even in a linear formulation, the PSE framework could suffer from limitations in the vicinity of the hump, resulting from the slowly-varying flow assumption. To avoid such modeling errors, the Adaptive Harmonic Linearized Navier-Stokes (AHLNS) framework was used as a

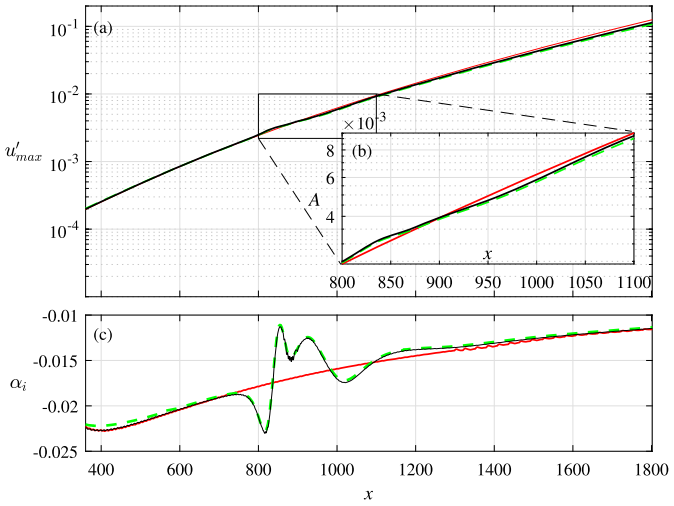

Fig. 10. Linear CFI amplitude development over the full domain (a), around the smooth hump (b), and growth rate (c) as calculated by the current HNS framework (solid, black), and the AHLNS (green, dashed). The flat-plate reference (i.e., no hump present) CFI amplitude development is shown in red.

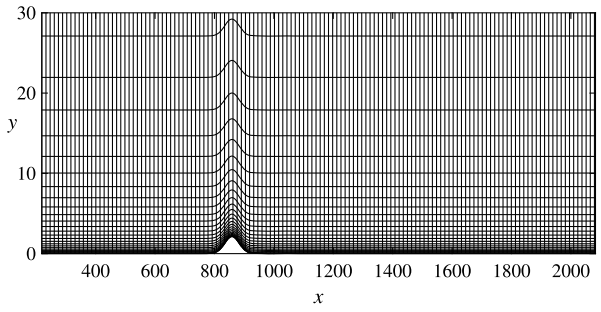

Fig. 11. Grid lines up to $y = 30$ indicated by the black lines. One in every fifteen ξ and one in every three η lines are shown.

reference. For linear computations, this tool is equivalent to the current HNS. The adaptivity of the AHLNS comes from the (re-)introduction of the streamwise wavenumber in the perturbation ansatz, to reduce the grid requirements when modal perturbation behavior is found. In contrast to PSE, however, no assumptions on the importance of higher-order streamwise gradients are made. For details on AHLNS, the reader is referred to Franco Sumariva et al. [23], Franco et al. [29].

The AHLNS calculations were provided by J.A. Franco and S. Hein of the German Aerospace Center (DLR) using the same base flow. Fig. 10 (a) shows the primary mode's linear amplitude evolution. A zoomed-in view of the amplitude development around the hump can be seen in Fig. 10 (b). A slight stabilization can be seen downstream of the hump. Nevertheless, the total effect on the amplitude is minimal. The growth rate as seen in Fig. 10 (c) shows the effect of the hump on the disturbance evolution and the good agreement between the two simulation frameworks. The small oscillations in all growth rate curves are an artifact of the calculation of growth rates from amplitude data.

6.4. Linear development of stationary crossflow instability over a forward-facing step

The difficulty of maintaining a laminar boundary layer in operational environments is partially caused by manufacturing limitations resulting in (critical) steps on the wing surface. The experiments of Perraud and Seraudie [80] and later Wang and Gaster [15] showed that the forward-facing step is less critical, i.e. less likely to advance transition than the backward-facing step for the same step height. When a step cannot be prevented at a junction, a forward-facing step becomes

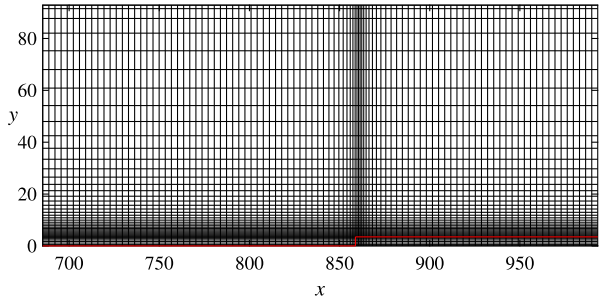

Fig. 12. Grid lines indicated in black. One in every forty ξ and one in every eight η lines are shown. The step surface is indicated in red.

the preferred solution as a result. The final validation case will therefore study the application of HNS to solve the stability problem of stationary CFI, interacting with a forward-facing step.

The flow around a step is complex and solving solely for either the base flow or its stability can be challenging. Specifically, separation bubbles can form both upstream and downstream of the step as shown by Wilhelm et al. [81] in two-dimensional flows. For the purpose of the present validation, the base flow, as well as the developed flow used here for comparison purposes, are produced using the conservative finite-volume solver INCA, described in Sect. 6.2. The case is based on the experiments of Rius-Vidales and Kotsonis [34] who performed a detailed experiment of the topological changes of the transitional flow field with a step compared to a reference case (i.e., no step).

One of the desired features of DeHNSSo is the ability to simulate non-homogeneous boundary conditions, which can be efficiently used in studies of receptivity or flow control. To demonstrate this functionality, a region of wall blowing and suction is employed slightly upstream of the step to force the dominant CFI mode. This steady blowing and suction has a sinusoidal spanwise dependence with a wavelength equal to that of the primary mode. The suction and blowing strength depends on the streamwise coordinate described by:

$$v_{\text{wall}}(x) = \begin{cases} A_{\text{bs}} \left(4 \, \frac{(x-x_1)-(x_2-x)}{(x_2-x_1)^2} \right)^3 & \text{if } x > x_1 \vee x < x_2 \\ 0 & \text{if } x \leq x_1 \vee x \geq x_2, \end{cases} \tag{28}$$

where the blowing and suction is active from $x_1 = 709$ to $x_2 = 738$ with a strength of $A_{\text{bs}} = 5 \times 10^{-5}$ defined as the imposed wall-normal peak velocity.

The simulation domain is defined by the intervals $x \in [685\ 993]$ and $y \in [0\ 89]$ with the Blasius length $\bar{\delta}_0 = 2.14 \times 10^{-4}$ m. The reference velocity is 15.1 m/s. This leads to a global $Re = 220$. The external velocity normal to the leading edge follows Eq. (26) with a constant spanwise velocity of $W_e = -1.24$. The buffer was initiated at 85% of the domain ($x = 947$).

The interaction of an incoming stationary CFI with a sharp forward-facing step results in strong local gradients that demand a finer grid than the previously described three cases. For the present case, a total of 4000 grid points were used in the streamwise direction, refined around the forward-facing step using a Gaussian function resulting in a minimum discretization step size $\Delta x_{\text{min}} = 2.1 \times 10^{-2}$ at the step and a $\Delta x_{\text{max}} = 8.5 \times 10^{-2}$ at 20 δ_0 away from the step. For reference, the streamwise wavelength upstream of the step is 40 $\bar{\delta}_0$. Therefore, there exist 469 grid points per wavelength in the coarse region. This is increased to approximately 2000 at the step. In the wall-normal direction, 350 collocation points were used. The collocation points were clustered around the step height throughout the domain with a $\Delta y_{\text{min}} = 3.37 \times 10^{-3}$ increasing to $\Delta y_{\text{min}} = 0.9$ at $y = 70$. This resulted in a grid of 1.4 million points. The grid is visualized in Fig. 12. It took DeHNSSo nearly 6 hours on 48 CPU cores (288 CPU core hours) to find the linear solution to the problem. INCA took 8.8 days on 2000 CPU cores (422400 CPU core hours) to find the solution. Moreover, INCA

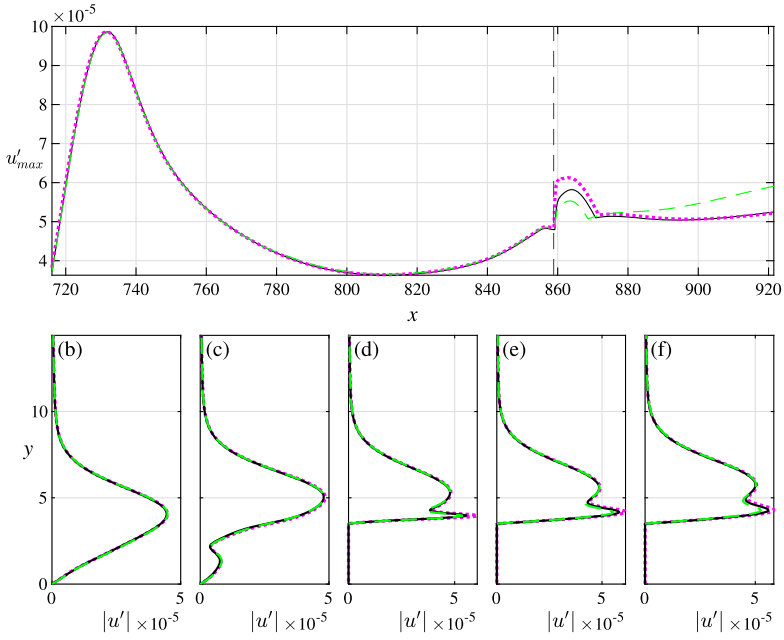

Fig. 13. Linear interaction of a stationary CFI initiated by blowing and suction around $x = 709$ and a forward-facing step present at $x = 738$, indicated by the dashed vertical line. Results are shown from DNS (magenta, dotted), HNS (black, solid), and AHLNS (green, dashed). Maximum perturbation amplitude development is shown in (a) and absolute streamwise perturbation shape is shown for $x =$ (b) 849, (c) 858, (d) 860, (e) 864, and (f) 867.

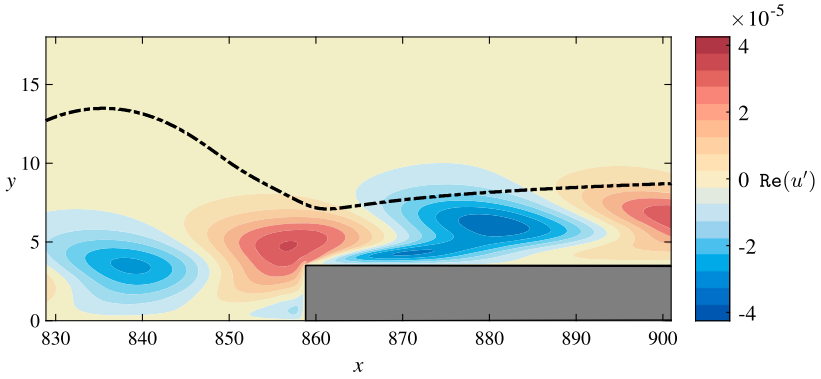

Fig. 14. Real streamwise perturbation velocity around the step with the dashed line indicating the δ_{99} of the base flow and the gray box represents the step.

solved the Navier-Stokes equations nonlinearly resolving an additional five higher harmonics, although they were found to be negligible due to their low amplitude.

Due to the large number of grid points required to converge this case, the choice was made to consider the linear development of the stationary crossflow instability governed by $\beta_1 = 0.18$ only. No amplitude ramping was thus necessary.

A comparison with DNS in terms of amplitude and shape functions can be seen in Fig. 13. It is noted that although the DNS did not neglect nonlinear terms, it was ensured that linear dynamics dominate the behavior of the perturbations by imposing a sufficiently small blowing and suction amplitude. Good agreement with DNS is seen in which a near-wall structure is accurately captured in the downstream vicinity of the step. This near-wall structure is important for both the local and downstream development of the incoming perturbation as was also found in similar cases experimentally in Eppink [19] and Rius-Vidales and Kotsonis [34] as well as numerically in Casacuberta et al. [33]. Fig. 14 shows the streamwise perturbation velocity contours of the primary mode around the step. Here, too, the near-wall structure is clearly observed slightly downstream of the step corner.

7. Concluding remarks

The present work outlines the development and implementation of an efficient non-linear Harmonic Navier-Stokes solver for the simulation of boundary layer and flow stability problems in complex geometrical domains. Smooth wall protuberances as well as local grid refinements are accounted for using a generalized domain transformation. Sharp geometries are accounted for through the use of embedded boundaries. The developed HNS solver proved accurate, fast, and robust in predicting the (non)linear stability of TS waves and stationary CFI developing on flat plate geometries or interacting with a localized hump or forward-facing step.

The developed HNS is envisioned to be a valuable tool for parametric studies of stability calculations in flows around steep humps, steps, and cases involving receptivity to inflow or wall forcing and non-modal growth. For these cases, PSE frameworks could fail to produce reliable and accurate results due to inherent assumptions of a slowly varying modal perturbation evolution. While DNS could be used to perform similar work, the high computational cost makes it impractical for many applications. The current implementation allows for rapid nonlinear stability analysis in flows featuring inhomogeneous bound-

Table A.1
Performance and system information for all considered cases.

Case	# Modes	$\Gamma_\xi \times \Gamma_\eta$	DOF/Mode	System	Cores	System Memory	Time
Nonlinear TS	5	800×40	128000	C	8	32 Gb	0.45 hours
Nonlinear TS Refined	5	2672×100	1155168	A	8	128 Gb	11.70 hours
Nonlinear CFI	5	1200×40	192000	C	8	32 Gb	1.29 hours
Nonlinear CFI Refined	5	2544×100	1017600	A	8	128 Gb	92.97 hours
Linear CFI Hump	1	2000×100	800000	C	4	32 Gb	0.59 hours
Linear CFI Step	1	4000×350	5600000	B	48	1.5 Tb	5.86 hours

ary conditions (e.g. blowing and suction), humps, and steps, enabling parametric studies of detailed wing geometries. The results can provide valuable insight into the interaction of incoming perturbations with surface features to further assist engineers and scientists in the pursuit of laminar wall-bounded flows.

CRediT authorship contribution statement

S. Westerbeek: Conceptualization, Data curation, Formal analysis, Investigation, Methodology, Software, Validation, Visualization, Writing – original draft, Writing – review & editing. **S. Hulshoff:** Supervision, Writing – original draft. **H. Schuttelaars:** Supervision, Writing – original draft. **M. Kotsonis:** Conceptualization, Software, Supervision, Writing – original draft, Funding acquisition, Writing – review & editing.

Declaration of competing interest

The authors declare that they have no known competing financial interests or personal relationships that could have appeared to influence the work reported in this paper.

Data availability

A link to both the data and code will be provided in the "attach file" step.

Acknowledgements

The authors would like to thank colleague J. Casacuberta for providing DNS results as a reference for various cases in this work. Similarly, we thank J.A. Franco and S. Hein of DLR Goetingen for providing the data required to validate the generalized domain in the validation case that featured a hump. Additionally, we are indebted to the technical staff of the DelftBlue supercomputer facility for providing the required computing power and systems. Lastly, the discussions and helpful comments of G. Rigas, Imperial College London are greatly appreciated. This research was funded by the European Research Council (ERC) under the GloWing project, grant number 803082.

Appendix A. Performance

This solver is meant to run simply and fast on regular desktop machines. As such, performance is evaluated here on similar architectures. The performance of the HNS is shown via Table A.1 containing the computational cost associated with solving the problems of Sect. 6. Both the requirements for the highly refined simulations necessary for validation and medium refinement are shown for the nonlinear simulations. The number of degrees of freedom per mode relates to the grid parameters as DOF/Mode $= \Gamma_\xi \times \Gamma_\eta \times 4$, where the constant is derived from the 4 state variables of velocity in x, y, and z and pressure.

A server workstation, here referred to as system A, features 2 Intel Xeon Gold 5222 CPUs operating at a clock speed of 3.8 GHz and 128 Gb of DDR4 Memory. However, note that for the cases in this work, only around 26 Gb was needed to solve the system of equations directly.

The interaction of a CFI with a step was assessed using the Delft High-Performance Computing Centre (DHPC) [82] 1.5 Tb memory node due to the high grid refinement required around the step. This node features 2 Intel XEON E5-6248R 24C for a total of 48 cores operating at a clock speed of 3.0GHz equipped with a total of 1.5 Tb of RAM. This system is referred to in Table A.1 as system B.

Lastly, the linear calculation of a crossflow instability over a hump was performed on a regular desktop computer. This system, referred to as system C, features an Intel(R) Xeon(R) W-2123 CPU @ 3.60GHz with 4 cores. The system is outfitted with a total of 32 Gb of DDR4 RAM.

Appendix B. Matrix contents

The nonlinear HNS equations, excluding the buffer matrix, can be written as:

$$[A]\mathbf{q} + [B]\omega\mathbf{q} + [C]\beta\mathbf{q} + [D]\beta^2\mathbf{q} + [E]\frac{\partial \mathbf{q}}{\partial \xi} + [F]\frac{\partial^2 \mathbf{q}}{\partial \xi^2} = \mathbf{r},$$

with

$$A = \begin{bmatrix} A_1 + \frac{\partial U}{\partial \xi}\xi_x + \frac{\partial U}{\partial \eta}\eta_x & \frac{\partial U}{\partial \xi}\xi_y + \frac{\partial U}{\partial \eta}\eta_y & 0 & \eta_x D_1 \\ \frac{\partial V}{\partial \xi}\xi_x + \frac{\partial V}{\partial \eta}\eta_x & A_1 + \frac{\partial V}{\partial \xi}\xi_y + \frac{\partial V}{\partial \eta}\eta_y & 0 & \eta_y D_1 \\ \frac{\partial W}{\partial \xi}\xi_x + \frac{\partial W}{\partial \eta}\eta_x & \frac{\partial W}{\partial \xi}\xi_y + \frac{\partial W}{\partial \eta}\eta_y & A_1 & 0 \\ \eta_x D_1 & \eta_y D_1 & 0 & 0 \end{bmatrix},$$

$$B = \begin{bmatrix} -i & 0 & 0 & 0 \\ 0 & -i & 0 & 0 \\ 0 & 0 & -i & 0 \\ 0 & 0 & 0 & 0 \end{bmatrix},$$

$$C = \begin{bmatrix} iW & 0 & 0 & 0 \\ 0 & iW & 0 & 0 \\ 0 & 0 & iW & i \\ 0 & 0 & i & 0 \end{bmatrix},$$

$$D = \begin{bmatrix} \frac{1}{Re} & 0 & 0 & 0 \\ 0 & \frac{1}{Re} & 0 & 0 \\ 0 & 0 & \frac{1}{Re} & 0 \\ 0 & 0 & 0 & 0 \end{bmatrix},$$

$$E = \begin{bmatrix} E_1 & 0 & 0 & \xi_x \\ 0 & E_1 & 0 & \xi_y \\ 0 & 0 & E_1 & 0 \\ \xi_x & \xi_y & 0 & 0 \end{bmatrix}$$

$$F = \begin{bmatrix} -\frac{1}{Re}\xi_x^2 - \frac{1}{Re}\xi_y^2 & 0 & 0 & 0 \\ 0 & -\frac{1}{Re}\xi_x^2 - \frac{1}{Re}\xi_y^2 & 0 & 0 \\ 0 & 0 & -\frac{1}{Re}\xi_x^2 - \frac{1}{Re}\xi_y^2 & 0 \\ 0 & 0 & 0 & 0 \end{bmatrix}$$

$$\mathbf{r} = \begin{bmatrix} -u\frac{\partial u}{\partial \xi}\xi_x - u\frac{\partial u}{\partial \eta}\eta_x - v\frac{\partial u}{\partial \xi}\xi_y - v\frac{\partial u}{\partial \eta}\eta_y - i\beta uw \\ -u\frac{\partial v}{\partial \xi}\xi_x - u\frac{\partial v}{\partial \eta}\eta_x - v\frac{\partial v}{\partial \xi}\xi_y - v\frac{\partial v}{\partial \eta}\eta_y - i\beta vw \\ -u\frac{\partial w}{\partial \xi}\xi_x - u\frac{\partial w}{\partial \eta}\eta_x - v\frac{\partial w}{\partial \xi}\xi_y - v\frac{\partial w}{\partial \eta}\eta_y - i\beta w^2 \\ 0 \end{bmatrix},$$

and

$$A_1 = U\eta_x \mathcal{D}_1 + V\eta_y D_1 - \frac{1}{Re}\left(\eta_x^2 D_2 + \eta_{xx} D_1 + \eta_y^2 D_2 + \eta_{yy} D_1\right),$$

$$E_1 = U\xi_x + V\xi_y - \frac{1}{Re}\xi_{xx} - \frac{1}{Re}2\eta_x\xi_x\frac{\partial}{\partial\eta} - \frac{1}{Re}2\eta_y\xi_y\frac{\partial}{\partial\eta} - \frac{1}{Re}\xi_{yy}.$$

Here the coordinate transformation derivatives are indicated using a subscript, for example $\frac{\partial\xi}{\partial x} = \xi_x$ and $\frac{\partial^2\eta}{\partial y^2} = \eta_{yy}$.

Appendix C. Left-hand side matrix

$$\mathbb{M}_1 = \begin{bmatrix} I & 0 & & & & \dots & 0 \\ -\frac{2E}{6\Delta x} + \frac{F}{(\Delta x)^2} & A - \frac{3E}{6\Delta x} - \frac{2F}{6(\Delta x)^2} & \frac{6E}{6\Delta x} + \frac{F}{(\Delta x)^2} & -\frac{E}{6\Delta x} & \ddots & & \\ \frac{E}{12\Delta x} - \frac{F}{12(\Delta x)^2} & -\frac{8E}{12\Delta x} + \frac{16F}{12(\Delta x)^2} & A - \frac{30F}{12(\Delta x)^2} & \frac{8E}{12\Delta x} + \frac{16F}{12(\Delta x)^2} & -\frac{E}{12\Delta x} - \frac{F}{12(\Delta x)^2} & & \\ \ddots & \ddots & \ddots & \ddots & \ddots & & \\ & \frac{E}{12\Delta x} - \frac{F}{12(\Delta x)^2} & -\frac{8E}{12\Delta x} + \frac{16F}{12(\Delta x)^2} & A - \frac{30F}{12(\Delta x)^2} & \frac{8E}{12\Delta x} + \frac{16F}{12(\Delta x)^2} & -\frac{E}{12\Delta x} - \frac{F}{12(\Delta x)^2} & \\ & & \frac{E}{6\Delta x} & -\frac{6E}{6\Delta x} + \frac{F}{(\Delta x)^2} & A - \frac{3E}{6\Delta x} - \frac{2F}{(\Delta x)^2} & \frac{2E}{6\Delta x} + \frac{F}{(\Delta x)^2} & \\ & \dots & 0 & \frac{E}{2\Delta x} + \frac{F}{(\Delta x)^2} & -\frac{4E}{2\Delta x} - \frac{2F}{(\Delta x)^2} & A + \frac{3E}{2\Delta x} + \frac{F}{(\Delta x)^2} & \end{bmatrix}$$

$$\mathbb{M}_2 = \begin{bmatrix} 0 & & \dots & 0 \\ & B & & \vdots \\ \vdots & & \ddots & 0 \\ 0 & \dots & 0 & B \end{bmatrix}, \quad \mathbb{M}_3 = \begin{bmatrix} 0 & & \dots & 0 \\ & C & & \vdots \\ \vdots & & \ddots & 0 \\ 0 & \dots & 0 & C \end{bmatrix},$$

$$\mathbb{M}_4 = \begin{bmatrix} 0 & & \dots & 0 \\ & D & & \vdots \\ \vdots & & \ddots & 0 \\ 0 & \dots & 0 & D \end{bmatrix}$$

References

[1] Ronald H. Radeztsky Jr, Mark S. Reibert, W.S. Saric, Effect of isolated micron-sized roughness on transition in swept-wing flows, AIAA J. 37 (11) (1999) 1370–1377.
[2] H.L. Reed, W.S. Saric, Stability of three-dimensional boundary layers, Annu. Rev. Fluid Mech. 21 (1) (1989) 235–284.
[3] W.S. Saric, H.L. Reed, E.B. White, Stability and transition of three-dimensional boundary layers, Annu. Rev. Fluid Mech. 35 (1) (2003) 413–440.
[4] I. Tani, Boundary-layer transition, Annu. Rev. Fluid Mech. 1 (1) (1969) 169–196.
[5] H.L. Reed, W.S. Saric, D. Arnal, Linear stability theory applied to boundary layers, Annu. Rev. Fluid Mech. 28 (1) (1996) 389–428.
[6] V. Theofilis, Global linear instability, Annu. Rev. Fluid Mech. 43 (2011) 319–352.
[7] L.M. Mack, Boundary-layer linear stability theory, Technical report, California Inst of Tech Pasadena Jet Propulsion Lab, 1984.
[8] C.E. Grosch, H. Salwen, The continuous spectrum of the Orr-Sommerfeld equation. Part 1. The spectrum and the eigenfunctions, J. Fluid Mech. 87 (1) (1978) 33–54.
[9] J.L. Van Ingen, The en method for transition prediction, Historical review of work at TU Delft. AIAA Paper, 3830:2008, 2008.
[10] J.L. Van Ingen, A suggested semi-empirical method for the calculation of the boundary layer transition region, Technische Hogeschool Delft, Vliegtuigbouwkunde, Rapport VTH-74, 1956.
[11] A.M.O. Smith, N. Gamberoni, Transition, pressure gradient and stability theory, Report ES 26388, Douglas Aircraft Co., 1956.
[12] F.P. Bertolotti, Th Herbert, P.R. Spalart, Linear and nonlinear stability of the Blasius boundary layer, J. Fluid Mech. 242 (1992) 441–474.
[13] Th. Herbert, Parabolized stability equations, agard r-793, 1993.
[14] B.J. Holmes, C.J. Obara, G.L. Martin, C.S. Domack, Manufacturing tolerances for natural laminar flow airframe surfaces, SAE Transact. (1985) 522–531.
[15] Y.X. Wang, M. Gaster, Effect of surface steps on boundary layer transition, Exp. Fluids 39 (4) (2005) 679–686.
[16] M.W. Tufts, H.L. Reed, B.K. Crawford, G.T. Duncan Jr, W.S. Saric, Computational investigation of step excrescence sensitivity in a swept-wing boundary layer, J. Aircr. 54 (2) (2017) 602–626.
[17] J.D. Crouch, V.S. Kosorygin, L.L. Ng, Modeling the effects of steps on boundary-layer transition, in: IUTAM Symposium on Laminar-Turbulent Transition, Springer, 2006, pp. 37–44.
[18] C. Edelmann, U. Rist, Impact of forward-facing steps on laminar-turbulent transition in subsonic flows, in: New Results in Numerical and Experimental Fluid Mechanics IX: Contributions to the 18th STAB/DGLR Symposium, Stuttgart, Germany, 2012, Springer, 2014, pp. 155–162.
[19] J.L. Eppink, Mechanisms of stationary cross-flow instability growth and breakdown induced by forward-facing steps, J. Fluid Mech. 897 (2020).
[20] A.F. Rius-Vidales, M. Kotsonis, Influence of a forward-facing step surface irregularity on swept wing transition, AIAA J. 58 (12) (2020) 5243–5253.
[21] T.S. Haynes, H.L. Reed, Simulation of swept-wing vortices using nonlinear parabolized stability equations, J. Fluid Mech. 405 (2000) 325–349.
[22] D. Park, S. Oh, Effect of shape of two-dimensional smooth hump on boundary layer instability, Int. J. Aeronaut. Space Sci. 21 (4) (2020) 906–923.
[23] J.A. Franco Sumariva, S. Hein, E. Valero, On the influence of two-dimensional hump roughness on laminar–turbulent transition, Phys. Fluids 32 (3) (2020) 034102.
[24] S. Westerbeek, J.A. Franco Sumariva, T. Michelis, S. Hein, M. Kotsonis, Linear and nonlinear stability analysis of a three-dimensional boundary layer over a hump, in: AIAA SCITECH 2023 Forum, 2023, p. 0678.
[25] M. Lessen, S.T. Gangwani, Effect of small amplitude wall waviness upon the stability of the laminar boundary layer, Phys. Fluids 19 (4) (1976) 510–513.
[26] C. Thomas, S.M. Mughal, M. Gipon, R. Ashworth, A. Martinez-Cava, Stability of an infinite swept wing boundary layer with surface waviness, AIAA J. 54 (10) (2016) 3024–3038.
[27] S. Westerbeek, M. Kotsonis, Effect of streamwise surface undulations on the nonlinear stability of crossflow instabilities. [unpublished manuscript], in: 12th International Symposium on Turbulence and Shear Flow Phenomena (TSFP12), 2022.
[28] A. Worner, U. Rist, S. Wagner, Humps/steps influence on stability characteristics of two-dimensional laminar boundary layer, AIAA J. 41 (2) (2003) 192–197.
[29] J.A. Franco, Stefan Hein, Eusebio Valero, Effect of humps and indentations on boundary-layer transition of compressible flows using the ahlns methodology, in: 7th European Conference on Computational Fluid Dynamics (ECFD 7-ECCOMAS), 2018.
[30] E.E. Cooke, M.S. Mughal, S. Sherwin, R. Ashworth, S. Rolston, Destabilisation of stationary and travelling crossflow disturbances due to steps over a swept wing, in: AIAA Aviation 2019 Forum, 2019, p. 3533.
[31] J. Casacuberta, S. Hickel, M. Kotsonis, Mechanisms of interaction between stationary crossflow instabilities and forward-facing steps, in: AIAA Scitech 2021 Forum, 2021, p. 0854.
[32] F. Tocci, J.A. Franco, S. Hein, G. Chauvat, A. Hanifi, The effect of 2-d surface irregularities on laminar-turbulent transition: a comparison of numerical methodologies, in: STAB/DGLR Symposium, Springer, 2020, pp. 246–256.
[33] J. Casacuberta, S. Hickel, S. Westerbeek, M. Kotsonis, Direct numerical simulation of interaction between a stationary crossflow instability and forward-facing steps, J. Fluid Mech. 943 (2022).
[34] A.F. Rius-Vidales, M. Kotsonis, Impact of a forward-facing step on the development of crossflow instability, J. Fluid Mech. 924 (2021).
[35] A.Y. Dobrinsky, Adjoint Analysis for Receptivity Prediction, Rice University, 2003.
[36] M. Choudhari, C. Streett, Theoretical prediction of boundary-layer receptivity, in: Fluid Dynamics Conference, 1994, p. 2223.
[37] C. Streett, Direct harmonic linear Navier-Stokes methods for efficient simulation of wave packets, in: 36th AIAA Aerospace Sciences Meeting and Exhibit, 1998, p. 784.
[38] Y. Guo, M. Malik, C.L. Chang, A solution adaptive approach for computation of linear waves, in: 13th Computational Fluid Dynamics Conference, 1997, p. 2072.
[39] Mark Carpenter, Meelan Choudhari, Fei Li, Craig Streett, Chau-Lyan Chang, Excitation of crossflow instabilities in a swept wing boundary layer, in: 48th AIAA Aerospace Sciences Meeting Including the New Horizons Forum and Aerospace Exposition, 2010, p. 378.
[40] Andrew Carpenter, William Saric, Helen Reed, Laminar flow control on a swept wing with distributed roughness, in: 26th AIAA Applied Aerodynamics Conference, 2008, p. 7335.
[41] L. Zhao, M. Dong, Y. Yang, Harmonic linearized Navier-Stokes equation on describing the effect of surface roughness on hypersonic boundary-layer transition, Phys. Fluids 31 (3) (2019) 034108.
[42] N. Hildebrand, M.M. Choudhari, P. Paredes, Predicting boundary-layer transition over backward-facing steps via linear stability analysis, AIAA J. 58 (9) (2020) 3728–3734.
[43] T. Appel, Boundary layer instabilities due to surface irregularities: a harmonic Navier-Stokes approach, Ph.D thesis, Imperial College London, 2020.
[44] I.B. de Paula, W. Würz, M.T. Mendonça, M.A.F. de Medeiros, Interaction of instability waves and a three-dimensional roughness element in a boundary layer, J. Fluid Mech. 824 (2017) 624–660.
[45] G. Rigas, D. Sipp, T. Colonius, Nonlinear input/output analysis: application to boundary layer transition, J. Fluid Mech. 911 (2021).
[46] K.C. Hall, J.P. Thomas, W.S. Clark, Computation of unsteady nonlinear flows in cascades using a harmonic balance technique, AIAA J. 40 (5) (2002) 879–886.
[47] D. Fabre, V. Citro, D. Ferreira Sabino, P. Bonnefis, J. Sierra, F. Giannetti, M. Pigou, A practical review on linear and nonlinear global approaches to flow instabilities, Appl. Mech. Rev. 70 (6) (2018).
[48] A. Lazarus, O. Thomas, A harmonic-based method for computing the stability of periodic solutions of dynamical systems, C. R., Méc. 338 (9) (2010) 510–517.
[49] A. Scholten, P. Paredes, M. Choudhari, F. Li, M. Carpenter, M. Bailey, Nonlinear nonmodal analysis of hypersonic flow over blunt cones, in: AIAA AVIATION 2023 Forum, 2023, p. 3420.
[50] Q. Song, L. Zhao, Scattering of mack modes by solid-porous junctions in hypersonic boundary layers, Phys. Fluids 34 (8) (2022) 084104.
[51] M.S. Kloker, U. Konzelmann, H. Fasel, Outflow boundary conditions for spatial Navier-Stokes simulations of transition boundary layers, AIAA J. 31 (4) (1993) 620–628.

[52] M. Israeli, S.A. Orszag, Approximation of radiation boundary conditions, J. Comput. Phys. 41 (1) (1981) 115–135.
[53] Daniel J. Bodony, Analysis of sponge zones for computational fluid mechanics, J. Comput. Phys. 212 (2) (2006) 681–702.
[54] J.P. Berenger, A perfectly matched layer for the absorption of electromagnetic waves, J. Comput. Phys. 114 (2) (1994) 185–200.
[55] T. Hagstrom, J. Goodrich, I. Nazarov, C. Dodson, High-order methods and boundary conditions for simulating subsonic flows, in: 11th AIAA/CEAS Aeroacoustics Conference, 2005, p. 2869.
[56] C. Liu, Z. Liu, Multigrid methods and high order finite difference for flow in transition-effects of isolated and distributed roughness elements, in: 11th Computational Fluid Dynamics Conference, 1993, p. 3354.
[57] J. Perraud, D. Arnal, A. Seraudie, D. Tran, Laminar-turbulent transition on aerodynamic surfaces with imperfections, ONERA: Tire a Part 13 (2004) 2004.
[58] S. Westerbeek, Development of a nonlinear parabolized stability equation (npse) analysis tool for spanwise invariant boundary layers, Msc thesis, 2020.
[59] Y.S. Kachanov, V.Y. Levchenko, The resonant interaction of disturbances at laminar-turbulent transition in a boundary layer, J. Fluid Mech. 138 (1984) 209–247.
[60] C.H. Bruneau, I. Mortazavi, Numerical modelling and passive flow control using porous media, Comput. Fluids 37 (5) (2008) 488–498.
[61] T. Michelis, C. de Koning, M. Kotsonis, On the interaction of Tollmien-Schlichting waves with a wall-embedded Helmholtz resonator, Phys. Fluids 35 (3) (2023).
[62] Peter J. Schmid, Linear stability theory and bypass transition in shear flows, Phys. Plasmas 7 (5) (2000) 1788–1794.
[63] M.I. Gavarini, Alessandro Bottaro, F.T.M. Nieuwstadt, Optimal and robust control of streaks in pipe flow, J. Fluid Mech. 537 (2005) 187–219.
[64] J.A. Weideman, S.C. Reddy, A Matlab differentiation matrix suite, ACM Trans. Math. Softw. 26 (4) (2000) 465–519.
[65] M.R. Malik, Numerical methods for hypersonic boundary layer stability, J. Comput. Phys. 86 (2) (1990) 376–413.
[66] C.L. Streett, M.G. Macaraeg, Spectral multi-domain for large-scale fluid dynamic simulations, Appl. Numer. Math. 6 (1–2) (1989) 123–139.
[67] R.D. Joslin, Validation of Three-Dimensional Incompressible Spatial Direct Numerical Simulation Code: A Comparison with Linear Stability and Parabolic Stability Equation Theories for Boundary-Layer Transition on a Flat Plate, vol. 3205, National Aeronautics and Space Administration, Office of Management . . . , 1992.
[68] M. Meyer, A. Devesa, S. Hickel, X.Y. Hu, Nikolaus A. Adams, A conservative immersed interface method for large-eddy simulation of incompressible flows, J. Comput. Phys. 229 (18) (2010) 6300–6317.
[69] F. Örley, V. Pasquariello, S. Hickel, N.A. Adams, Cut-element based immersed boundary method for moving geometries in compressible liquid flows with cavitation, J. Comput. Phys. 283 (2015) 1–22.
[70] J. Casacuberta, K.J. Groot, Q. Ye, S. Hickel, Transitional flow dynamics behind a micro-ramp, Flow Turbul. Combust. 104 (2) (2020) 533–552.
[71] E.B. White, W.S. Saric, Secondary instability of crossflow vortices, J. Fluid Mech. 525 (2005) 275–308.
[72] J.P. Boyd, Chebyshev and Fourier Spectral Methods, Courier Corporation, 2001.
[73] C.L. Chang, M. Malik, G. Erlebacher, M. Hussaini, Linear and nonlinear pse for compressible boundary layers, 1993.
[74] Th Herbert, Parabolized stability equations, Annu. Rev. Fluid Mech. 29 (1) (1997) 245–283.
[75] G. Zoppini, S. Westerbeek, D. Ragni, M. Kotsonis, Receptivity of crossflow instability to discrete roughness amplitude and location, J. Fluid Mech. 939 (2022).
[76] S. Hickel, N.A. Adams, Implicit les applied to zero-pressure-gradient and adverse-pressure-gradient boundary-layer turbulence, Int. J. Heat Fluid Flow 29 (3) (2008) 626–639.
[77] St Hickel, C.P. Egerer, J. Larsson, Subgrid-scale modeling for implicit large eddy simulation of compressible flows and shock-turbulence interaction, Phys. Fluids 26 (10) (2014) 106101.
[78] A.V. Boiko, A.V. Dovgal', V.V. Kozlov, V.A. Shcherbakov, Flow instability in the laminar boundary layer separation zone created by a small roughness element, Fluid Dyn. 25 (1) (1990) 12–17.
[79] COMSOL Multiphysics® v. 5. 6 user guide, COMSOL AB, 2022.
[80] J. Perraud, A. Seraudie, Effects of steps and gaps on 2d and 3d transition, in: European Congress on Comp. Methods in Applied Science and Eng., ECCOMAS, 2000, pp. 11–14.
[81] D. Wilhelm, C. Härtel, L. Kleiser, Computational analysis of the two-dimensional–three-dimensional transition in forward-facing step flow, J. Fluid Mech. 489 (2003) 1–27.
[82] Delft High, Performance computing centre (DHPC). DelftBlue supercomputer (phase 1), https://www.tudelft.nl/dhpc/ark:/44463/DelftBluePhase1, 2022.